SYNTHETIC APERTURE SILHOUETTE IMAGING FOR SPACE DOMAIN AWARENESS

THESIS

Lester L. Tuck IV, Captain, USSF

AFIT-ENY-MS-22-M-314

DEPARTMENT OF THE AIR FORCE
AIR UNIVERSITY

AIR FORCE INSTITUTE OF TECHNOLOGY

Wright-Patterson Air Force Base, Ohio

DISTRIBUTION STATEMENT A
APPROVED FOR PUBLIC RELEASE; DISTRIBUTION UNLIMITED.

AFIT-ENY-MS-22-M-314

SYNTHETIC APERTURE SILHOUETTE IMAGING FOR SPACE DOMAIN AWARENESS

THESIS

Presented to the Faculty
Department of Aeronautics and Astronautics
Graduate School of Engineering and Management
Air Force Institute of Technology
Air University
Air Education and Training Command
in Partial Fulfillment of the Requirements for the
Degree of Master of Science in Astronautical Engineering

Lester L. Tuck IV, B.S.A.E.
Captain, USSF

March 24, 2022

AFIT-ENY-MS-22-M-314

SYNTHETIC APERTURE SILHOUETTE IMAGING FOR SPACE DOMAIN AWARENESS

THESIS

Lester L. Tuck IV, B.S.A.E.
Captain, USSF

Committee Membership:

Andrew S. Keys, Ph.D
Chair

Lt Col Bryan D. Little, Ph.D
Member

Carl R. Hartsfield, Ph.D
Member

AFIT-ENY-MS-22-M-314

Abstract

The increasing interest in cislunar space as a new orbital regime for artificial satellites exceeds the traditional imaging capabilities used to enable some aspects of Space Domain Awareness, an issue present even at Geostationary Equatorial Orbit (GEO) distances. Synthetic Aperture Silhouette Imaging (SASI), which resolves a silhouette of a space object using ground based measurements of the diffraction pattern cast by the object's occultation of a distant stellar light source, provides a new method that may be used to characterize these satellites. Reverse propagation of the diffraction pattern with use of a phase retrieval algorithm leads to the reconstruction of a silhouette from only intensity diffraction distribution measurements. This research analyzes the reconstruction of satellite silhouettes using data from a scaled benchtop experiment to evaluate the distance and resolution limitations of Synthetic Aperture Silhouette Imaging at distances equal to and beyond GEO. Diffraction patterns of two scaled satellite silhouette targets are captured at various scaled distances. The laboratory data is fed to Matlab code which utilizes an iterative Gerchberg-Saxton phase retrieval algorithm to estimate the original silhouettes. The reconstructed silhouettes are compared to the original 'truth' silhouettes to estimate the resolution at each distance. Resolutions of 36 centimeters at GEO altitude and 1.54 meters at twice GEO altitude were obtained. Refinements to further data collection and processing are analyzed and show potential for even greater resolution. These results demonstrate the value of SASI as a tool which can provide valuable information of a satellite of interest, filling in a current Space Domain Awareness imaging capability gap.

Acknowledgements

I would like to express my profound appreciation for my faculty advisor, Dr. Andrew S. Keys, without whose insight and guidance this thesis would not be possible. I would also like to express my sincere gratitude for Dr. Peter N. McMahon-Crabtree, both for his insight and his silhouette reconstruction code which served as a linchpin in this analysis. Finally, I would like to thank my wife, Melanie Tuck, for her everlasting love, support, and patience during the long days and nights required on this research. Without her I would not be where I am today.

Lester L. Tuck IV

Table of Contents

Page

List of Figures

List of Tables

Table Page

SYNTHETIC APERTURE SILHOUETTE IMAGING FOR SPACE DOMAIN AWARENESS

I. Introduction

1.1 Background and Motivation

The increasing interest in cislunar space as a new orbital regime for artificial satellites exceeds the traditional imaging capabilities used to enable some aspects of Space Domain Awareness (SDA). This is an issue already present at GEO distances, where an object's small angular subtense requires extremely large apertures and very good atmospheric conditions to be imaged from the ground, even with advanced imaging capabilities such as adaptive optical systems [1]. A 180 meter telescope with adaptive optics is required for a 10 centimeter resolution at GEO distances, far beyond reasonable expense with modern capabilities [2]. Satellite characteristics beyond simple tracking, such as state of deployable structures, attitude determination, and rendezvous and proximity operation information, are all details critical to robust SDA which typically require some form of imaging to assess with confidence.

Synthetic Aperture Silhouette Imaging (SASI), which resolves a satellite's silhouette using ground based measurements of the diffraction pattern cast by an occluded distant stellar light source, provides a new method that may be used to characterize these high altitude satellites, and its use for GEO satellites was proposed by Burns, et al. [1]. SASI shows advantages over existing ground-based imaging while providing information comparable to imaging of a lower altitude satellite. The nature of the diffraction imaging data required for SASI results in a reduced cost on a fielded system through use of inexpensive telescopes and photodetectors. Additionally, the mathematics behind Fresnel diffraction, used for SASI, results in an imaging capability that is resistant to atmospheric disturbance [2]. Non-reliance on the target's visual magnitude, which is important for traditional imaging methods, is another benefit of SASI, which relies on the magnitude of the occluded star (which produces the diffraction pattern ground shadow), rather than the object of interest itself [3]. The benefits over traditional imaging and the potential to fill a capability gap begs the question of how SASI may be used for SDA.

1.2 Research Objectives

This research focuses on silhouette reconstruction at distances equal to and beyond GEO, and aims to identify the limitations of the reconstruction process using laboratory data. The research questions that were investigated are as folllows:

1. How can data be gathered in the laboratory that is equivalent to SASI measurements taken on the ground of GEO and beyond satellites?
    (a) Construct a scaled benchtop experiment that captures diffraction images of a satellite.
2. What are the distance and resolution limitations of SASI measurements of GEO and beyond satellites?
    (a) Reconstruct satellite silhouettes using diffraction data from benchtop experiments.
    (b) Analyze resolution limits at various scaled distances leading up to and beyond GEO.

3. What, if any, improvements to the diffraction capture and silhouette reconstruction process may improve imaging resolution?
    (a) Identify techniques or equipment that may improve results from SASI measurements.
    (b) Implement improvements into benchtop experiment and re-assess, or evaluate analytically.

1.3 Document Overview

This document is organized as follows. Chapter II provides an overview of relevant background information and a review of existing literature regarding SASI. Chapter III details the process of constructing the scaled benchtop experiment, collection of diffraction data, and reconstruction of satellite silhouettes. Chapter IV presents the results of evaluating reconstructed data for resolution limitations and any implemented SASI improvements. Finally, Chapter V discusses the conclusions drawn from the results as well as recommendations for future work regarding SASI experiment improvements and further research towards a fielded SASI system.

II. Background and Literature Review

2.1 Synthetic Aperture Silhouette Imaging

Synthetic Aperture Silhouette Imaging, or SASI, relies on the convenient ever-present nature of stars as a light source, albeit with inherent difficulty in alignment between star, target satellite, and ground observation. SASI's use for GEO satellites was first proposed as "Shadow Imaging of GEO Satellites" by Burns et al. in 2005 [1]. When a satellite occults a star, which is a nearly ideal point source, a shadow is cast on the surface of the Earth, which can be detected using a radiometric telescope through measuring the change in irradiance [1, 4]. Even GEO satellites, relatively stationary overhead, will cast these shadows which move west to east on the Earth's surface as the distant stars move across behind them [4]. The light passing around the satellite diffracts, however, and the resulting pattern is the shadow seen at the Earth's surface. An array of telescopes arranged north-south can capture and measure this intensity diffraction distribution as a function of time, which can be reconstructed into the satellite's silhouette using an iterative phase retrieval algorithm [1]. A diagram of the SASI concept is shown in Figure 1. A SASI array would not require advanced imagers, with even inexpensive hobby telescopes and low-cost APD detectors viable for the technique [3]. Additionally, the intensity diffraction measurement provides SASI an advantage where an obstacle exists for other ground-based imaging techniques; limitations due to atmospheric turbulence are avoided, as the measured Fresnel amplitude is insensitive to turbulence near the imager (the case for space observations from the ground) [3]. Along with these benefits, information obtained from SASI is comparable to that of traditional imagers. Deployable status, vehicle orientation, solar array size and deployment, and number and type of payloads, are all potentially gathered from a simple resolved silhouette. These factors combine to highlight the potential value of SASI as a tool to fill the imaging gap in our Space Domain Awareness [2].

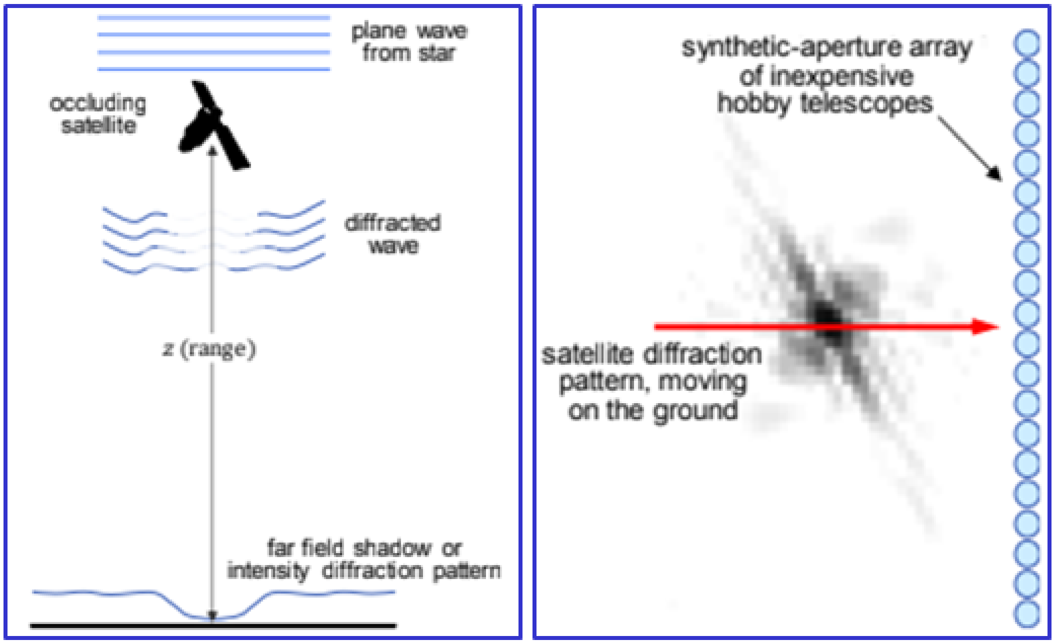

Figure 1: Depiction of the SASI concept, where light from a distant star is occluded by a satellite of interest, creating a moving intensity diffraction pattern which is imaged with an array of inexpensive telescopes [3].

2.2 Fresnel Diffraction

Due to the relative distances and sizes of a stellar light source, a satellite of interest, and an observation from Earth's surface, light from a stellar source can be approximated to originate at infinity. Light passing through an aperture (in our case, around a satellite) is diffracted by the edges and results in a light intensity distribution which propagates according to the Huygens-Fresnel principle as the light continues to travel, shown in Figure 2. For a complex object at great distances, such as a satellite in GEO, the resulting intensity distribution is unrecognizable as the diffracting object. Thus, the original silhouette must be reconstructed, which is possible using the principles of diffraction.

The Huygens-Fresnel principle is given by (1) and (2), where in our case $U(\xi,\, \eta)$ is the complex field distribution at the plane just past the satellite silhouette, $U(x,\, y)$ is the complex scalar field distribution at the imaging array (the magnitude of which is the square of the measured intensity), the distance z is the satellite's altitude, and $k = 2\pi/\lambda$ [5].

$$U(x,y) = \frac{z}{j\lambda} \iint_{\Sigma} U(\xi,\eta) \frac{\exp jkr}{r^2} d\xi d\eta \tag{1}$$

$$r = \sqrt{z^2 + (x-\xi)^2 + (y-\eta)^2} \tag{2}$$

To reconstruct the satellite silhouette, simplification of (1) is desirable. To do so, the Fresnel approximation is used, which is valid for an observation taken in the near field, and allows an accurate prediction of the resulting intensity distribution [5]. To evaluate the validity of the Fresnel approximation, the Fresnel number is determined, which is used as a coarse approximation of the division between the near and far fields [5]. In general, if the Fresnel number is approximately greater than one, the

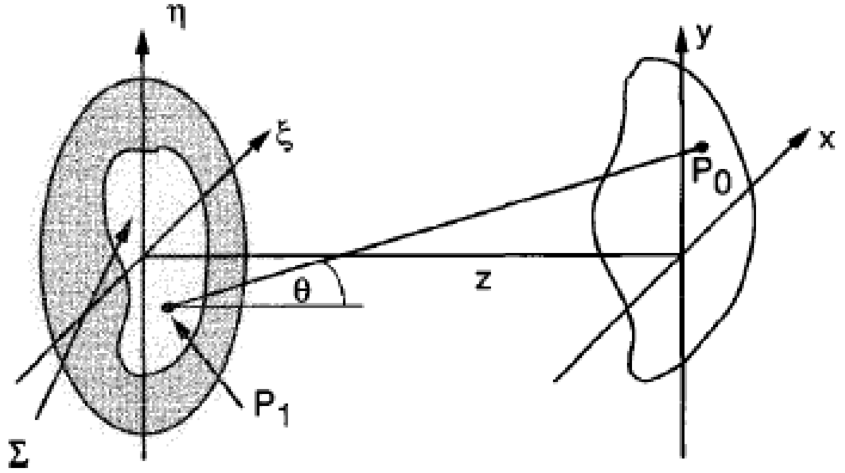

Figure 2: Diffraction from an aperture in the ξ-η plane, propagating in the positive z direction, observed in the x-y plane [5].

observation is in the near field, and if approximately less than one, the observation is in the far field. The Fresnel number for an Earth-based observation of a 5 m by 10 m GEO satellite is given by (3)

$$F = \frac{w^2}{\lambda z} = \frac{5 * 10}{500\text{x}10^{-9} * 36\text{x}10^{6}} = 2.5 \tag{3}$$

where w is the characteristic size of the aperture, λ is the wavelength of the light source, and z is the propagation distance. The length and width of the satellite is used as the characteristic size squared to determine an overall Fresnel number, but note that in reality the length and width of the satellite have separate Fresnel numbers that may cause the diffraction in those dimensions to be better or worse predicted by the Fresnel approximation. For λ, 550 nm is used as the approximate center of the visible spectrum. The result is a Fresnel number of 2.5, thus, light from a stellar source diffracting around a satellite in GEO observed from the ground is predictably described by the Fresnel approximation. It is clearly seen that maintaining the other variables and increasing the propagation distance will decrease the Fresnel number, thus, future research into observations at even greater distances, i.e. observations in the far field, can instead use the Fraunhofer approximation.

The Fresnel approximation is based on the binomial expansion of (2) [5]. After factoring z out of the square root, the binomial expansion is given by

$$r \approx z\left[1+\frac{1}{2}\left(\frac{x-\xi}{z}\right)^2+\frac{1}{2}\left(\frac{y-\eta}{z}\right)^2\right] \tag{4}$$

The r in the denominator of (1) is replaced by only the first term of this approximation, since the error introduced by dropping all but the first term is small [5]. However, the approximated r in the exponential retains all terms since even miniscule phase changes can significantly change the exponential [5]. The Fresnel approximation then becomes

$$U(x,y)=\frac{e^{jkz}}{j\lambda z}\iint_{-\infty}^{\infty} U(\xi,\eta)\exp\left\{j\frac{k}{2z}\left[(x-\xi)^2+(y-\eta)^2\right]\right\}d\xi d\eta \tag{5}$$

By factoring $\exp\frac{jk}{2z}(x^2+y^2)$ out of the integral, the result is easily seen in (6) as a Fourier transform of the product of the complex field just past the aperture, and a quadratic phase exponential, along with some multiplicative factors [5]. Thus, by measuring the diffraction intensity, retrieving the unknown phase (using a phase retrieval algorithm) and an inverse Fourier transform, we can arrive at an estimation of the original silhouette.

$$U(x,y)=M\iint_{-\infty}^{\infty}\left[U(\xi,\eta)\exp\left\{j\frac{k}{2z}\left(\xi^2+\eta^2\right)\right\}\right]\exp\left\{-j\frac{2\pi}{\lambda z}(x\xi+y\eta)\right\}d\xi d\eta \tag{6}$$

$$M=\frac{e^{jkz}}{j\lambda z}\exp j\frac{k}{2z}(x^2+y^2) \tag{7}$$

Through observation of (5), it can be easily seen that the equation is scalable by multiplying the object and image plane dimensions by an arbitrary factor, γ, and the distance between the object and imaging plane by γ^2 [3]. The preceding complex exponential is unimportant, since again the measurement is of intensity and the unknown phase is solved for with an algorithm.

$$U(\gamma x, \gamma y) = \frac{\gamma^2 e^{jk\gamma^2 z}}{j\lambda\gamma^2 z} \iint_{-\infty}^{\infty} U(\gamma\xi, \gamma\eta) \exp\left\{ j\frac{k\gamma^2}{2\gamma^2 z} \left[(x-\xi)^2 + (y-\eta)^2 \right] \right\} d\xi d\eta \tag{8}$$

$$U(\gamma x, \gamma y) = \frac{e^{jk\gamma^2 z}}{j\lambda z} \iint_{-\infty}^{\infty} U(\gamma\xi, \gamma\eta) \exp\left\{ j\frac{k}{2z} \left[(x-\xi)^2 + (y-\eta)^2 \right] \right\} d\xi d\eta \tag{9}$$

As an example, a 10 m object at GEO distance (36e6 m) results in the same diffraction pattern as a 1 mm object at a distance of 36 cm. Thus lies the basis for the laboratory experiment in this research.

2.3 Previous Works

The 2005 Burns et al. work [1] laid the foundation for the use of SASI for GEO satellites. The data collection method and silhouette reconstruction using diffraction measurements were described and an initial analysis was performed using simulated data at various levels of SNR, which showed a promising level of resolution at GEO [1]. Additionally, the problem of usable star density was assessed through graphs of star visual magnitude vs. star density, occultation opportunity, and SNR, and predicted an 86% chance of total occultation with SNR greater than 5 if a 10 to 20 km long rail track is used to mount the imaging array [1]. An analysis of required array precision is also provided, and concludes that current satellite ephemerides are nowhere near the required array positioning of +/- 15 m, although a solution is proposed in the form of a two-stage process whereby the satellite position is more accurately acquired with a single astrometric telescope before prepositioning the array for the diffraction intensity capture [1]. These two main problems have yet to be fully mastered, although others have provided additional analysis.

The desired signal to noise ratio for a SASI measurement sets a limit on the required star visual magnitude, which in turn limits the number of useable stars [1]. This star density can be examined through either a measure of the numbers of shadows cast at a particular location on the Earth, or the measure of all shadows cast by a particular satellite [6]. A star catalog, used to compare against satellite positions, requires high levels of positional accuracy when developing star density maps. This alignment challenge, combined with the inaccuracy of TLE data, results in one of the largest obstacles for SASI methods [6]. The capability of mapping the density of shadows cast by satellites was developed by Douglas et al. [6] for use in the optimization problem of SASI system placement. An example of such a shadow density map is shown in Figure 3, and revealed promising results, with between 800 and 2000 shadows cast by one GEO satellite at any point in the night when limiting latitude between -55 and 55 degrees, viewing elevation angle greater than 30 degrees, and star visual magnitude between 2 and 10 [6]. Results also showed that shadow rates significantly increase as star visual magnitude decreases. This solution space was further explored by Sheppard et al. in 2017 and 2018, [7, 8], with the 2017 work using data from the Raven small telescope systems on Maui to compare against predictions at a single site from a TLE-based tool, and additionally included two shadow density maps of a single GEO satellite 10 days apart. The shadow density maps revealed a northern hemisphere bias for shadow distribution, and that the shadow produced by a satellite-star pair is present night-to-night, with a km offset between nights, which was observed by Paxman in 2016 [2, 7]. The 2018 Sheppard et al. work further examined validation of shadow track prediction using Raven data, and finds TLE data insufficient for use in a SASI system, with the north-south shadow track error noted as the key ‘missing link‘, which is closely related to cross-track error in satellite tracking [8]. Also produced was a cost-function weighted global shadow density map using 315 GEO satellites, shown in Figure 4, identifying the optimal site as a location on the Ethipia/Djibouti border and decreasing with longitude and latitude further from this location [8].

Another issue is that the placement of the telescope array used to capture an occultation event requires a north-south precision greater than currently obtainable by using traditional two-line element data [1, 8]. An exceptionally long array of telescopes can be used to overcome this deficiency, requiring an array nearly a kilometer long, but another solution exists, in which a smaller, moveable array is placed on a railroad track, convoy, or sea platform, which may be more economical [1, 4]. A single telescope with an intensified camera may also be used to measure the target satellite position to

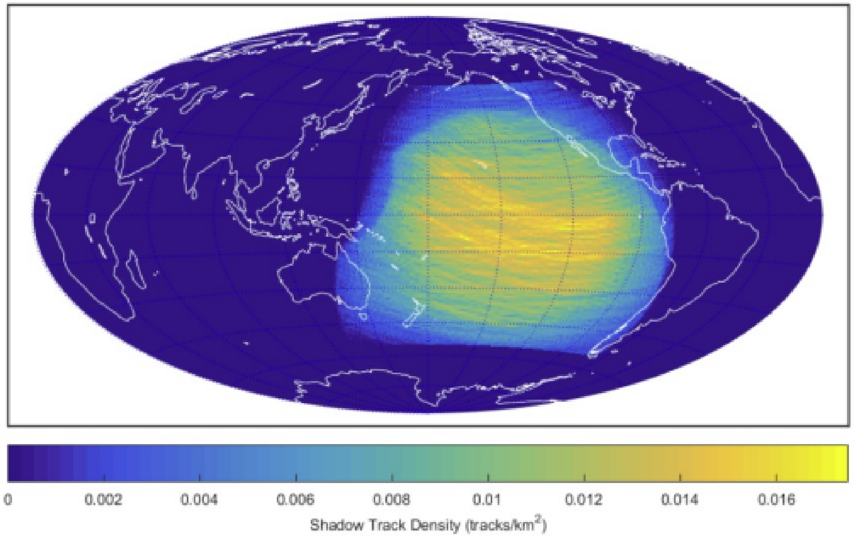

Figure 3: Shadow density map for GEO satellite Galaxy 3C on night of Jan. 19th, 2016, created by Douglas et al. in 2016 [6].

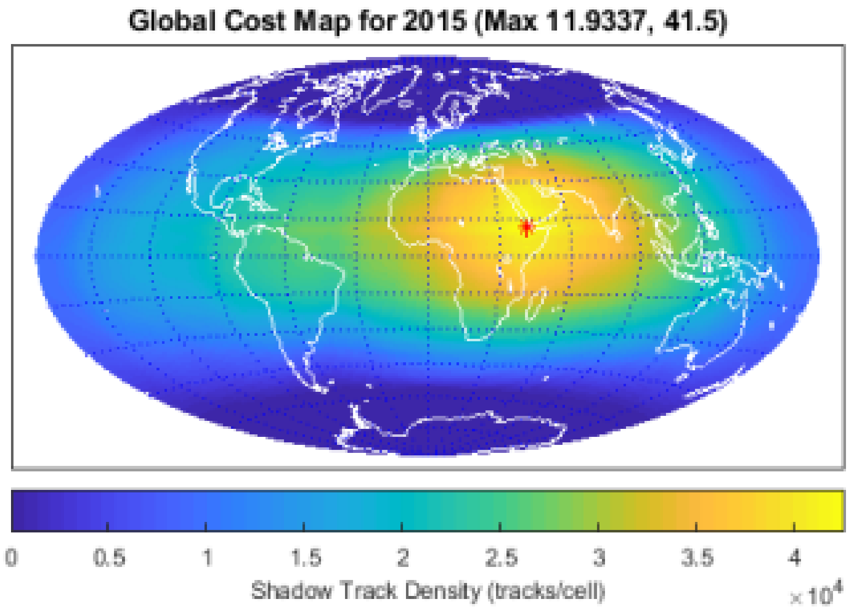

Figure 4: Cost-function weighted shadow density map using 315 GEO satellites, created by Sheppard et al. in 2018 [8].

greater accuracy and allow the array to move to the correct location for an observation [1]. While these concepts have been proposed by others, they have not been analyzed in detail, however the logistics are relatively simple and may be more suited for analysis when a fielded system is fully proposed.

Analysis conducted by others, mainly through simulated data, has aided in proving the concept of SASI and providing various methods for improving the results [2, 4, 8, 9, 10]. Paxman in 2016 [2] performed a simple proof-of-concept simulation of phase retrieval using an opacity constraint by Fourier transforming a silhouette truth image. The amplitude from this Fourier transform was then used in an iterative phase retrieval algorithm, which was able to perfectly retrieve the silhouette [2]. Douglas et al. performed a similar, independent analysis in 2016 [6] by using a shadow simulation capability that generates monochromatic and spectrally binned irradiance patterns with various SNRs. These shadow simulations were used as the input to an iterative phase retrieval algorithm to reconstruct the truth silhouettes, which resulted in sub-meter resolution at GEO, and showed that resolution can be improved by a factor of 2 when aperture size is halved (given sufficient SNR) [6]. Douglas et al. in 2017 [11] derived resolution limits for SASI of GEO satellites, both through simulation and analytically as a function of spectral bin width and aperture size. The analytic results showed a linear increase in resolution limit with increasing spectral bin width, as well as with increasing aperture diameter, along with the important result that SASI resolution limits are much less sensitive to central wavelength and object distance than traditional imaging methods [11]. The simulated silhouette reconstructions showed resolution limits very close to the analytical results, with sub-meter results obtainable at GEO using small (20 to 40 cm) apertures [11]. This reversal of traditional imaging requirements, where larger apertures are required for increased resolution, is a substantial cost benefit to SASI as a tool for SDA.

Spectrally resolved SASI, a technique introduced by Luu et al. in 2008 [4] uses arrays of detectors capturing light from different wavelengths as a means of increasing spatial resolution, compensating for the smearing of the diffraction pattern caused by a broadband source. The work used simulated data to compare shadow images using bandpass filters with different bandwidths to a shadow image constructed from a sum of 10 narrowband images, and showed the resultant broadband image has a resolution equivalent to the narrowband resolution [4]. Image reconstructions from simulated data performed by Douglas et al. [6] confirmed that higher resolution can be obtained through separating measurements into spectral bins, with narrower bins providing higher resolution [6]. The same reconstructions showed an increase in resolution from smaller aperture sizes, at the cost of requiring brighter stars [6]. The result is an optimization problem of aperture size and spectral bin width combinations to obtain the highest resolution [6].

A general formalism for determining the position of a knife edge occulting a star by using its Fresnel diffracted pattern was developed by McNicholl and Crabtree in 2014 [10] who addressed the statistical bounds and maximum-likelihood estimator performance. The work also analyzed spectrally resolved SASI, and found a measurable but small increase (a factor of 2 to 3) on resolution [10]. With the results from Luu et al. and Douglas et al. [4, 6] the question of how much spatial resolution can actually be obtained from spectrally resolved real SASI measurements has has yet to be answered with real data, which is invaluable to weighing costs during the proposal of a fielded SASI system.

In 2020 Paxman et al. [3] became the first to use laboratory data to demonstrate silhouette reconstruction from Fresnel intensity diffraction. The benchtop setup used a 3200K color temperature high-intensity illuminator, with a 40 nm spectral filter centered at 650 nm, spatial filter assembly, and collimating lens to illuminate a helicopter target on a microscope slide, and captured the resulting diffraction pattern with a 4656 x 3522 format, 6 μm^2 pixel pitch, CCD camera [3]. The target slide was positioned at a distance on the bench scaled to GEO equivalent distance, and emulated a linear array of 30 cm telescopes placed 60 cm apart by using non-adjacent binned pixels in camera [3]. Using the prior knowledge that the silhouette is binary, which is likely to be the case for most space objects, the reconstructed image resolution, shown in Figure 5, traced to a 35 cm resolution on a GEO satellite, even with phase abberations induced by the microscope slide (which would not be present in a field collection) [3].

Finally, although no field experiments have been conducted using SASI for Earth satellites, occultation measurements of deep space astronomical objects have been used in the scientific community for many years with startling results [12, 13].

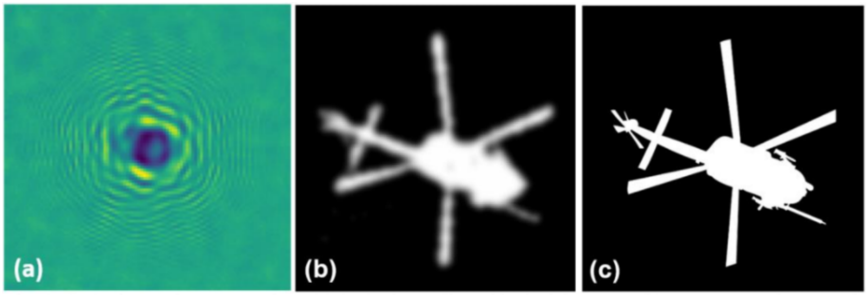

Figure 5: (a) SASI laboratory data, (b) reconstructed image, and (c) truth silhouette, collected by Paxman in 2020 [3].

III. Methodology

By means of the scaling described in Section 2.2, and with Paxman's 2020 lab demo [3] as a template, a benchtop experiment is constructed to capture the diffraction pattern of a satellite silhouette, which is then used to reconstruct the original silhouette through reverse propagation. This chapter describes the benchtop experiment setup, data collection methodology, and silhouette reconstruction process of the research.

3.1 Benchtop Experiment Setup

Figure 6 shows the layout of the benchtop experiment used to capture the Fresnel diffraction pattern of a satellite silhouette. From right to left are the three light sources, spatial filter assembly, collimating lens, target containing the silhouettes, and camera used for data collection.

3.1.1 Equipment Overview

The primary light source for the experiment is a ThorLabs HNL020LB 632.8 nm helium-neon laser with a 0.59 mm beam width, however the setup is constructed to allow captures with either the primary or one of two additional sources; ThorLabs

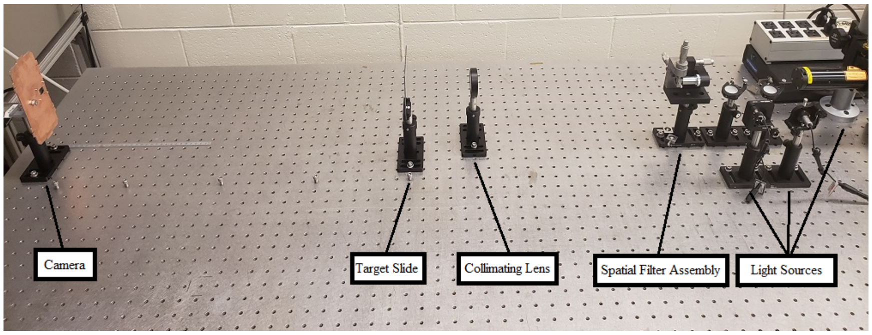

Figure 6: Benchtop experiment layout, including light sources, spatial filter, collimating lens, target, and camera.

CPS532 and CPS450 laser diodes with 532 nm and 450 nm wavelengths, respectively, shown in Figure 7. Due to time constraints, only the 632.8 nm source is used for this research. The spatial filter assembly is composed of a Newport M Series objective lens and a Newport 900 Series high-energy pinhole. The lens used for collimation is a 2 in diameter lens with 400 mm focal length. The target is a 0.0625 inch thick, 4 by 4 inch soda lime glass with a chrome mask containing two satellite silhouettes, a GPS Block III-A satellite and a Soyuz TMA-7 spacecraft, chosen for their variety of feature sizes, each approximately 900 by 600 µm. The camera used to collect the data is a ThorLabs Zelux CS165CU with 3.45 μm^2 pixel size, and images are captured in 1440 x 1080 16-bit grayscale format.

3.1.2 Spatial Filter

To provide a beam with a smooth intensity profile to the collimating lens, a spatial filter assembly is used to remove spatial noise from output beam of the laser sources,

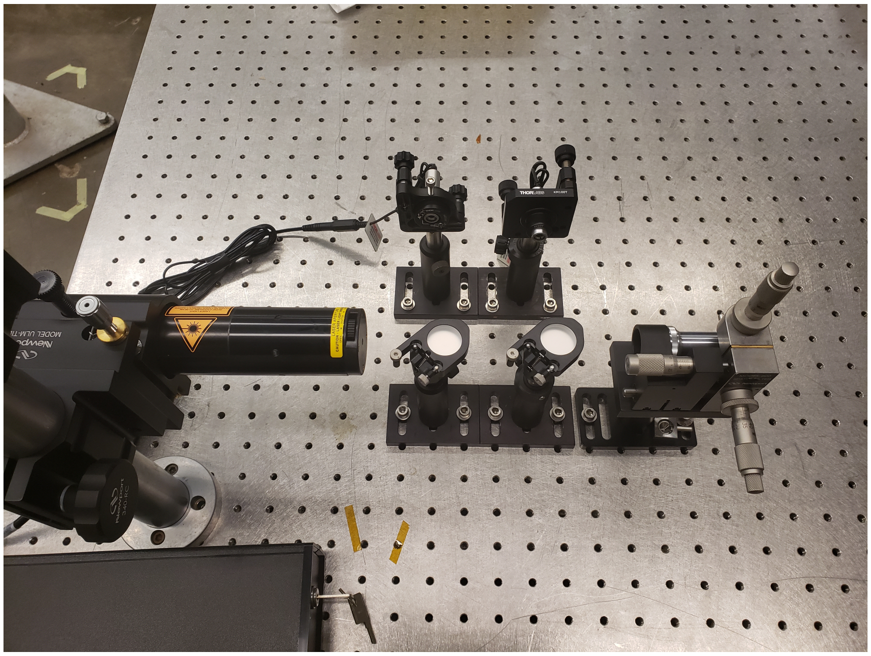

Figure 7: Primary and additional light sources, flip-up mirrors in lowered positions. Also shown: spatial filter assembly.

and consists of a microscope objective lens, pinhole, and 3-axis mount, shown in Figure 8. The objective lens is either 10X magnification or 40X magnification, and the pinhole is either a 5 µm, 10 µm, or 15 µm, depending on the light source used. The optimal pinhole size is determined using (10), where λ is the beam wavelength, D is the beam diameter, and f is the focal length of the objective lens [14]. This optimizes the amount of energy passed while limiting spatial noise as much as possible [14]. The objective lens is chosen for each laser source to require an optimal pinhole as close as possible to what is available in the laboratory. The result is a 40X magnification lens and 10 µm pinhole for the 632.8 wavelength laser, a 10X magnification lens and 5 µm pinhole for the 532 wavelength laser, and a 10X magnification lens and 15 µm pinhole for the 450 wavelength laser, summarized in Table 1.

$$\text{Pinhole Diameter} = 1.5 \times 1.27\frac{\lambda f}{D} \tag{10}$$

3.1.3 Collimating Lens

After passing the spatial filter, the beam is passed through a collimating lens in order to approximate a source at infinity, i.e. the assumption used for a stellar source occulted by an artificial satellite. The collimating lens is initially placed in the path of the beam approximately 400 mm (the focal length of the lens) down range of the spatial filter assembly. A shear plate is used to check for a well-collimated beam, and

Table 1: Selected Spatial Filter Components

Source Wavelength (nm)	**Objective Magnification**	**Optimal Pinhole (μm)**	**Selected Pinhole (μm)**
632.800	40 X	9.194	10.000
532.000	10 X	4.778	5.000
450.000	10 X	14.145	15.000

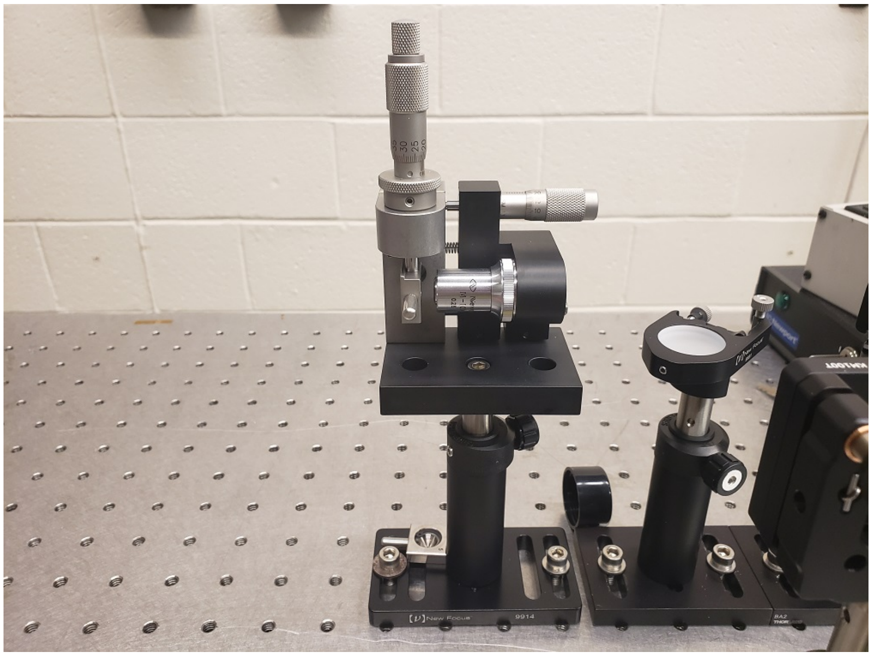

Figure 8: Spatial filter assembly consisting of microscope objective lens, pinhole, and 3-axis mount.

small adjustments are made to the location and alignment of the collimating lens if necessary. This process is repeated after any changes are made to the spatial filter assembly.

3.1.4 Target

The well-collimated beam exiting the collimating lens is occluded by one of the silhouettes on the target, which then produces a diffraction pattern that propagates down range. The silhouettes on the target are spaced apart such that only one target can occlude the beam at a time. Microscope images of the silhouettes are shown in Figure 9, and the images used by AFIT's Photolithography lab to create them are shown in Figure 10. The distance between the camera imaging plane and the silhouette on the target is the desired propagation distance for the measurement, shown in Figure 11.

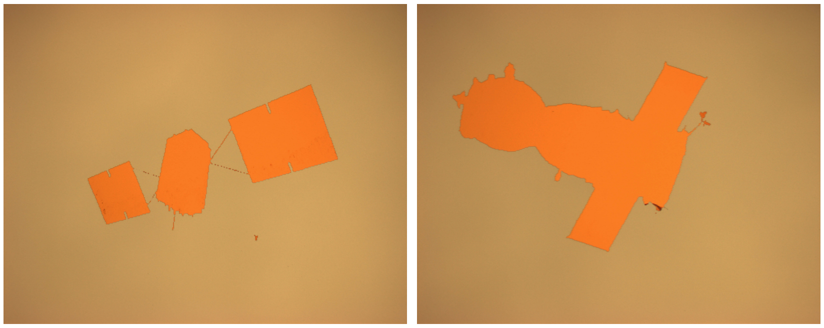

Figure 9: Microscope images of the GPS (left) and Soyuz (right) targets.

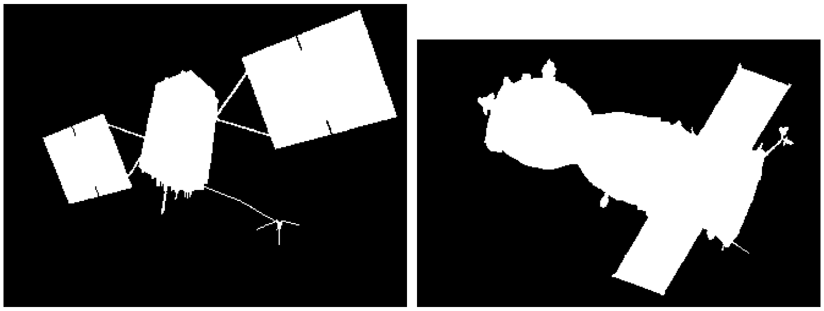

Figure 10: GPS (left) and Soyuz (right) image files used to create the target slide.

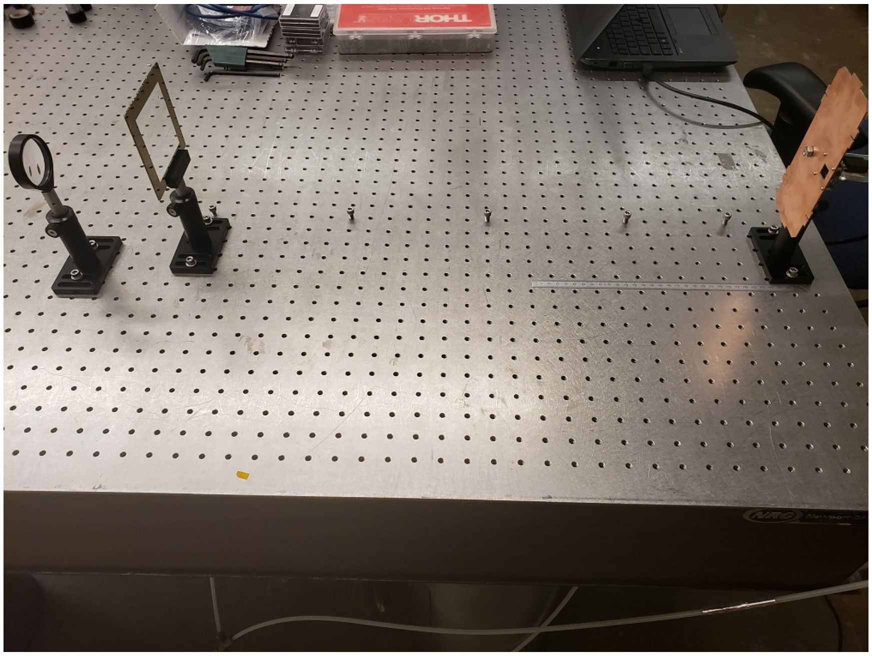

Figure 11: Collimating lens, target, and camera. The diffraction propagation distance is the distance between the camera imaging plane and the silhouette on the target.

3.2 Data Collection

To collect an image of the satellite silhouette's diffraction pattern, the source laser is chosen and the flip-up mirrors are configured to pass the desired source. If required, the spatial filter is re-assembled according to Table 1 and the beam is checked for collimation. Software for the ThorLabs Zelux CS165CU camera is started on the laboratory computer and the live view is used to verify camera functionality and that the 1440 by 1080 16-bit grayscale image format is selected. The target mount is placed at the desired diffraction propagation distance, measured out from the camera imaging plane and adjusted in the vertical and transverse range directions until the diffraction pattern is seen in the center of the imaging software's live view. Images are taken at five distances, using a scaling factor, γ, of 10^4 as prescribed by (8), shown in Table 2. The 53.4 mm distance, used as an attempted baseline, is the shortest distance that the benchtop experiment can physically accomodate, and the multiples of GEO are used in an effort to determine how the resolution is impacted at great distances, as the focus of the research is on imaging of GEO and greater distances. To limit noise, overhead lights in the laboratory are turned off and the computer monitor is turned to direct its light away from the camera. The real-time histogram on the camera software is then used to adjust the integration time on the camera to ensure there is no pixel saturation. The diffraction image is saved along with a flat field image with the target removed and a dark field image with the laser turned off. The flat and dark field images assist with removing noise during the reconstruction process. The entire process is then repeated for the additional desired propagation distances. An example of the resultant diffraction pattern is shown in Figure 12.

Table 2: Benchtop Experiment Distance Scaling

Reference Orbital Distance	Scaled Distance Simulated (km)	Benchtop Experiment Distance (mm)
MEO	5340	53.4
0.5x GEO	18040	180.4
GEO	35820	358.2
1.5x GEO	53600	536.0
2.0x GEO	71380	713.8

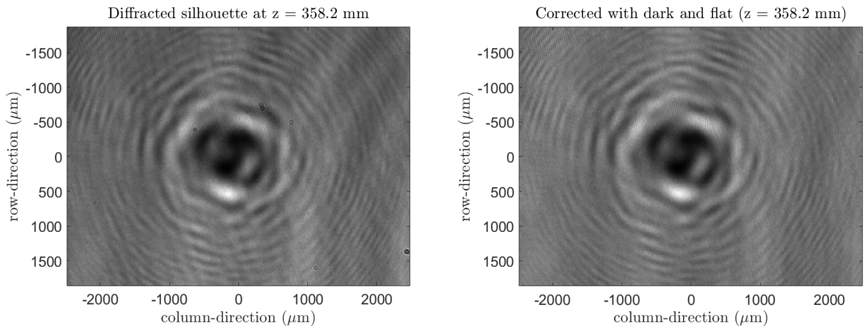

Figure 12: Diffraction pattern image output from the benchtop experiment, with and without correction using dark and flat field images.

3.3 Silhouette Reconstruction

To reconstruct the satellite silhouette, Matlab code created by Dr. McMahon-Crabtree of AFRL/RV is used with the captured images as inputs. The program incorporates a modified Gerchberg-Saxton phase-retrieval algorithm and reverse Fresnel propagates the diffraction pattern to estimate the true silhouette. Since the light source used is a red HeNe laser and the imaging device is a color camera, the input images are modified to keep only red pixels. The program then calibrates the image using the dark and flat field as well as simple gaussian filtering to reduce noise and mitigate unwanted artifacts, such as diffraction from lens defects or dust. A comparison between results with and without this pre-filtering is provided at the output. Additional program options include the use of zero padding around the diffraction image and the number of iterations in the phase-retrieval algorithm. The Matlab code is used to reconstruct the images at each distance using eight different values of zero padding: first with no zero padding, then zero pad to 720 x 720, 874 x 874, 1024 x 1024, 1536 x 1536, 2048 x 2048, 3072 x 3072, and 4096 x 4096. Early calibration of the code revealed a significant effect of zero padding on the resultant reconstructions, thus an analysis at various zero padding levels is desired. The largest amount of zero padding is chosen as a trade off between processing time and maximum expected desirable zero padding, determined from the early calibration. The other amounts of zero padding are convenient factors of two and amounts halfway between the factors of two. A user-selectable mask is used as a support constraint, defining the maximum object extent, and is also used as the initial object estimate in the iterative phase retrieval algorithm. An example of the program output, before final adjustments were made to the code and format of the output, is shown in Figure 13.

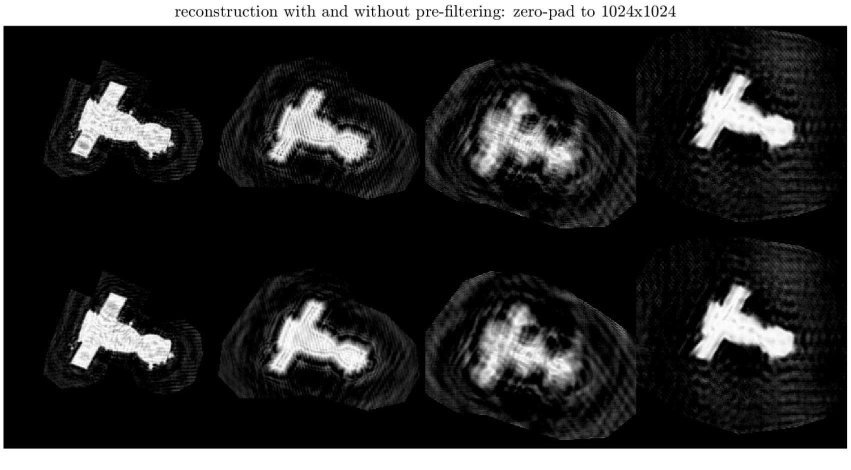

Figure 13: Example output during calibration of the silhouette reconstruction code, where diffraction images at four different distances (left to right: 9 mm, 40 mm, 100 mm, 358 mm) were processed simultaneously. Top images are without pre-filtering, bottom images are with pre-filtering.

IV. Results and Analysis

This chapter contains images of the laboratory collected data and the subsequent reconstructions for the GPS and Soyuz satellite targets, and an analysis of the results. By comparing the various features of the GPS and Soyuz silhouette reconstructions, using the zero padding amount that provides the most resolved image, to the target images in Figure 9, and referencing the size of features using the silhouette images in Figure 10, an estimate of the resolution at each distance is obtained. Each pixel in the silhouette image is measured as one micron on the target slide, which scales to 1 cm in orbit. Section 4.1 breaks down the results at each distance while mentioning unique or notable results, and section 4.2 summarizes the results and analyzes trends.

4.1 Laboratory Data and Silhouette Reconstructions

Figure 14 shows the images captured at a distance of 53.4 mm (5340 km altitude equivalent), used as inputs to the Matlab code whose silhouette reconstruction results with eight amounts of zero padding are shown in Figure 15 and Figure 16. Captured laboratory images at the four other distances will be shown without flat field and dark frame, as they provide little for this analysis, but are available in Appendix A.

The silhouette reconstructions at this distance are far more noisy than those of the larger distances. Spatial frequency noise is seen in the reconstructions with each amount of zero padding, and does not allow clear resolution of any smaller feature of the Soyuz, although the general form of the two silhouettes are visible. This may be due to a resonance between the spatial frequency noise and the diffraction patterns in the input images. This can be seen in the collected data, as some of the spatial frequency noise and diffraction pattern have fringes spaced roughly equally apart. The reconstructions for both satellites are most resolved beginning at 1536 x 1536 zero padding, and do not improve with larger amounts of zero padding.

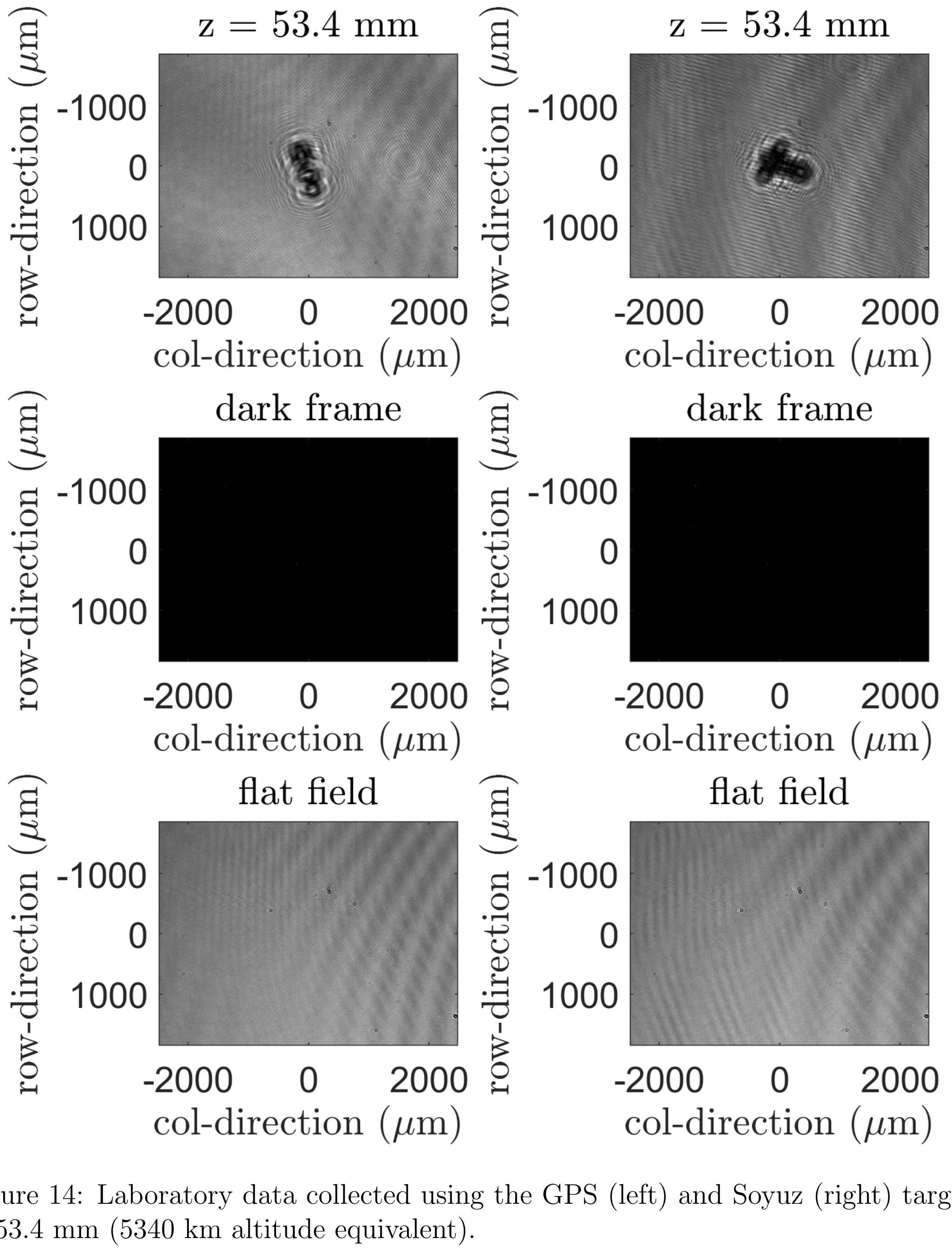

Figure 14: Laboratory data collected using the GPS (left) and Soyuz (right) targets at 53.4 mm (5340 km altitude equivalent).

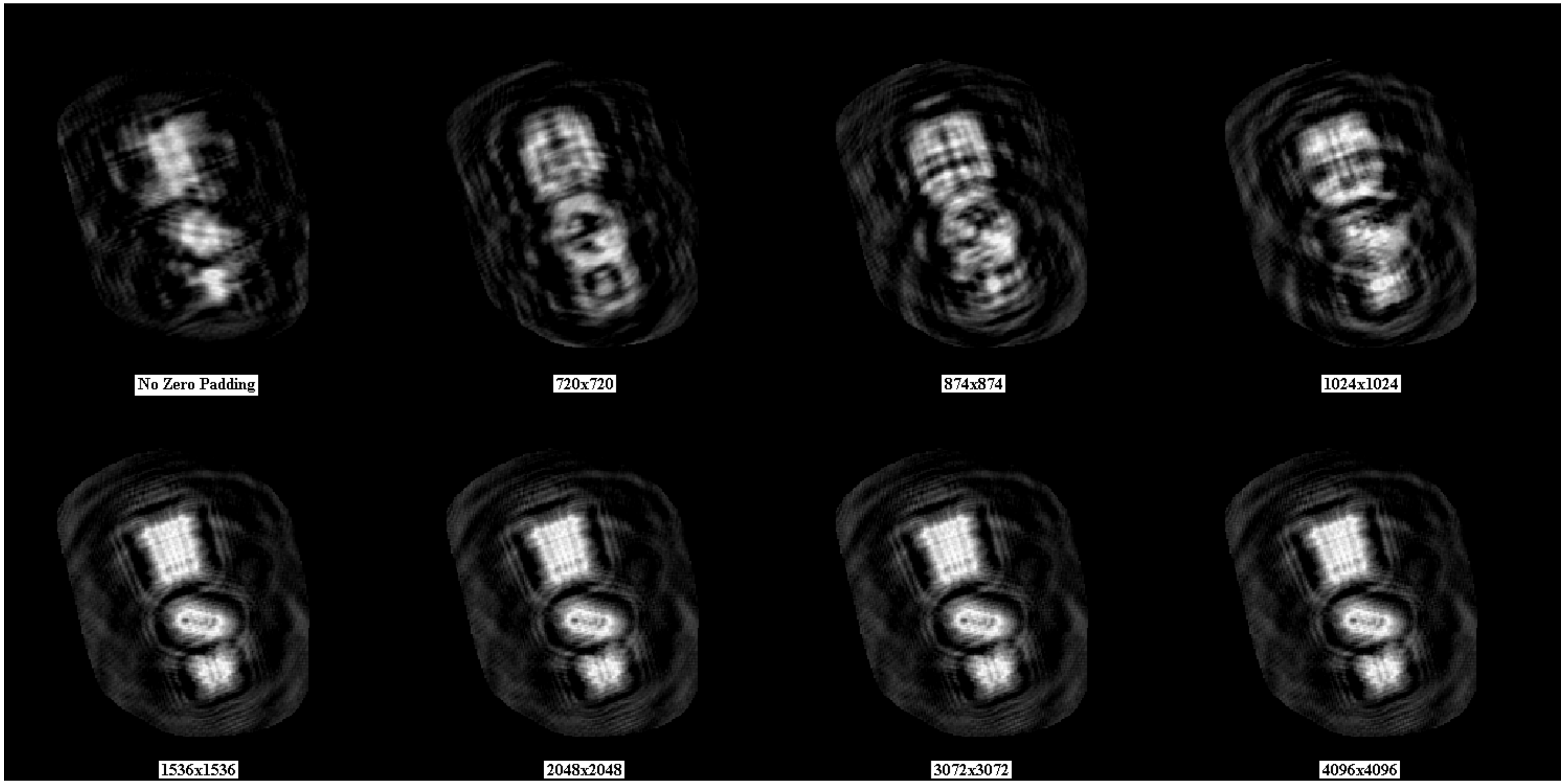

Figure 15: Silhouette reconstruction of the GPS satellite at 53.8 mm (5340 km altitude equivalent) using eight different amounts of zero padding, shown below each reconstruction.

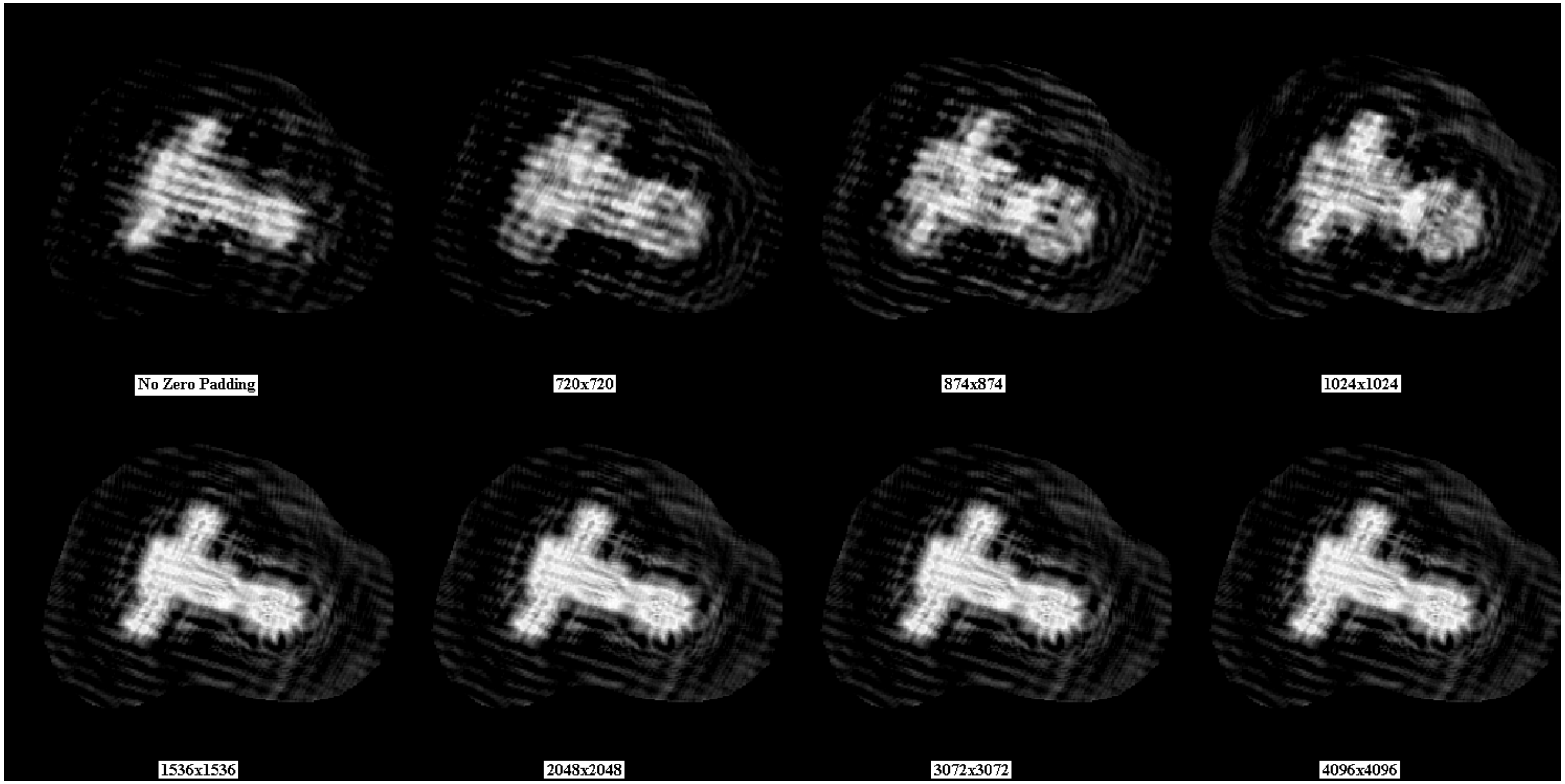

Figure 16: Silhouette reconstruction of the Soyuz spacecraft at 53.8 mm (5340 km altitude equivalent) using eight different amounts of zero padding, shown below each reconstruction.

Figure 17 shows the images captured at a distance of 180.4 mm (0.5x GEO altitude equivalent), used as inputs to the Matlab code whose silhouette reconstruction results with eight amounts of zero padding are shown in Figure 18 and Figure 19.

The silhouette reconstructions at this distance are very clear at the zero padding amount of 1536 x 1536, with even small instruments and antennas of the Soyuz spacecraft visible. All other amounts of zero padding are significantly less clear. Edges and corners of the GPS satellite and Soyuz spacecraft solar panels and main body are very sharp. The small (3 micron/scaled 3 cm) separations in the middle of the GPS solar panels are not fully resolvable, but do appear as slight breaks in the sharp edges of the solar panels. Inspecting the smallest resolvable features on the bottom right of the Soyuz spacecraft, the resolution at this distance is estimated to be 24 microns (scaled 24 cm).

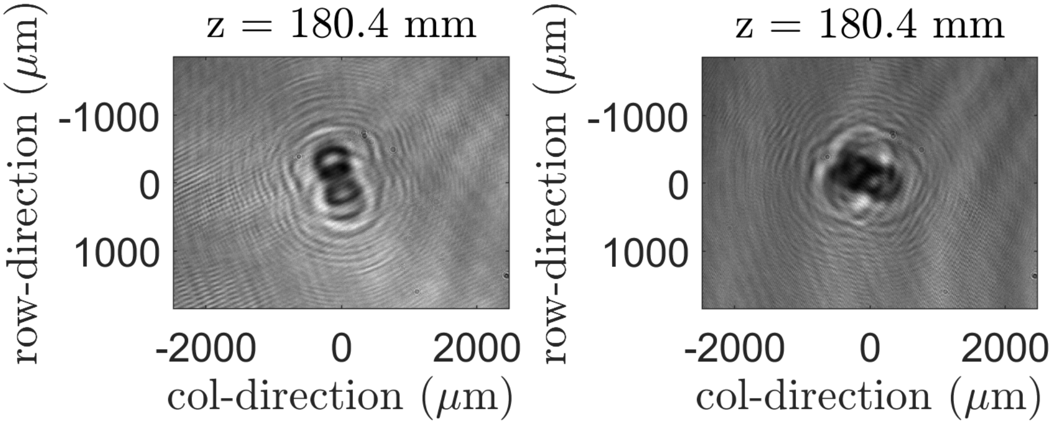

Figure 17: Laboratory data collected using the GPS (left) and Soyuz (right) targets at 180.4 mm (0.5x GEO altitude equivalent).

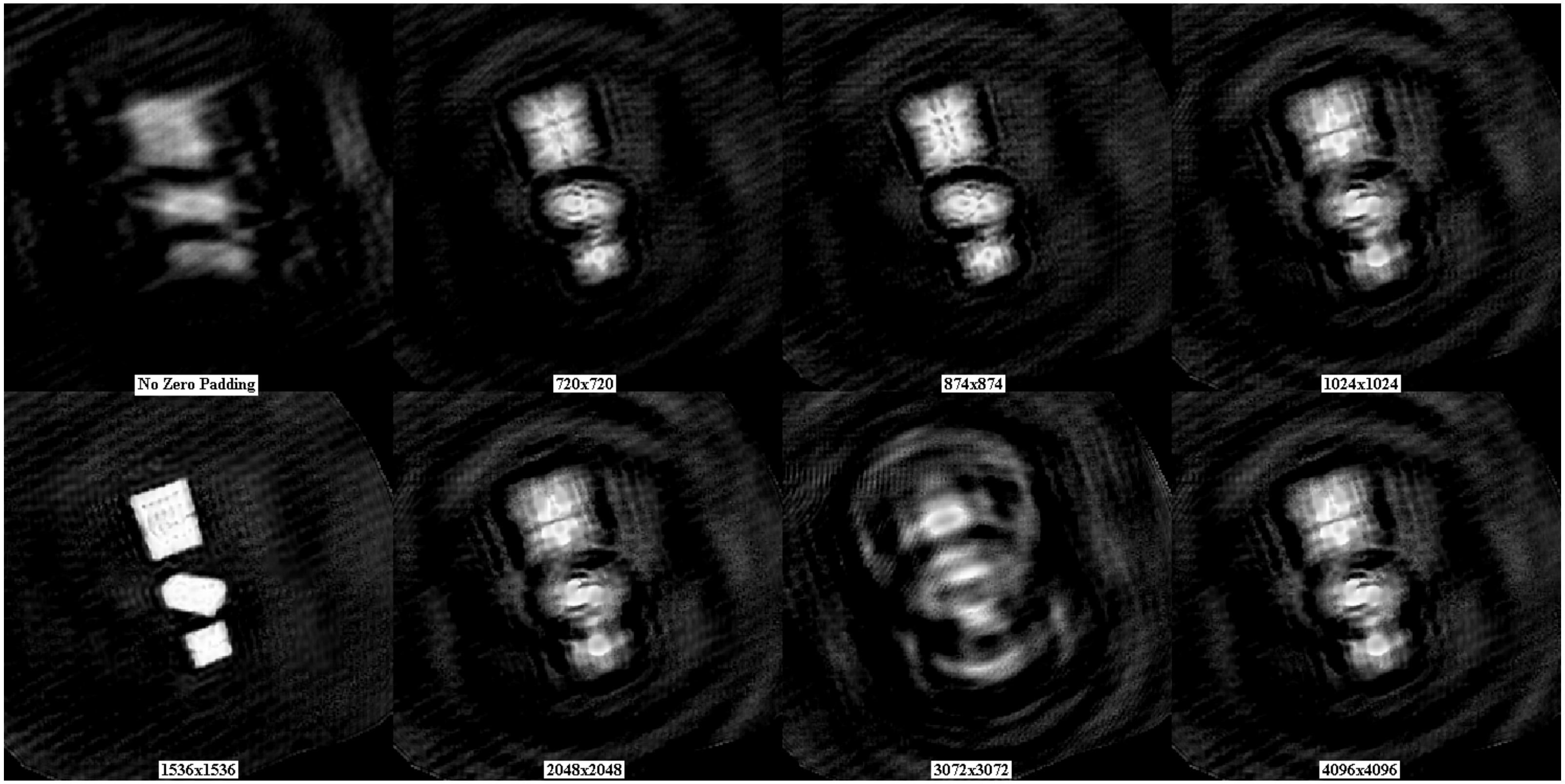

Figure 18: Silhouette reconstruction of the GPS satellite at 180.4 mm (0.5x GEO equivalent) using eight different amounts of zero padding, shown below each reconstruction.

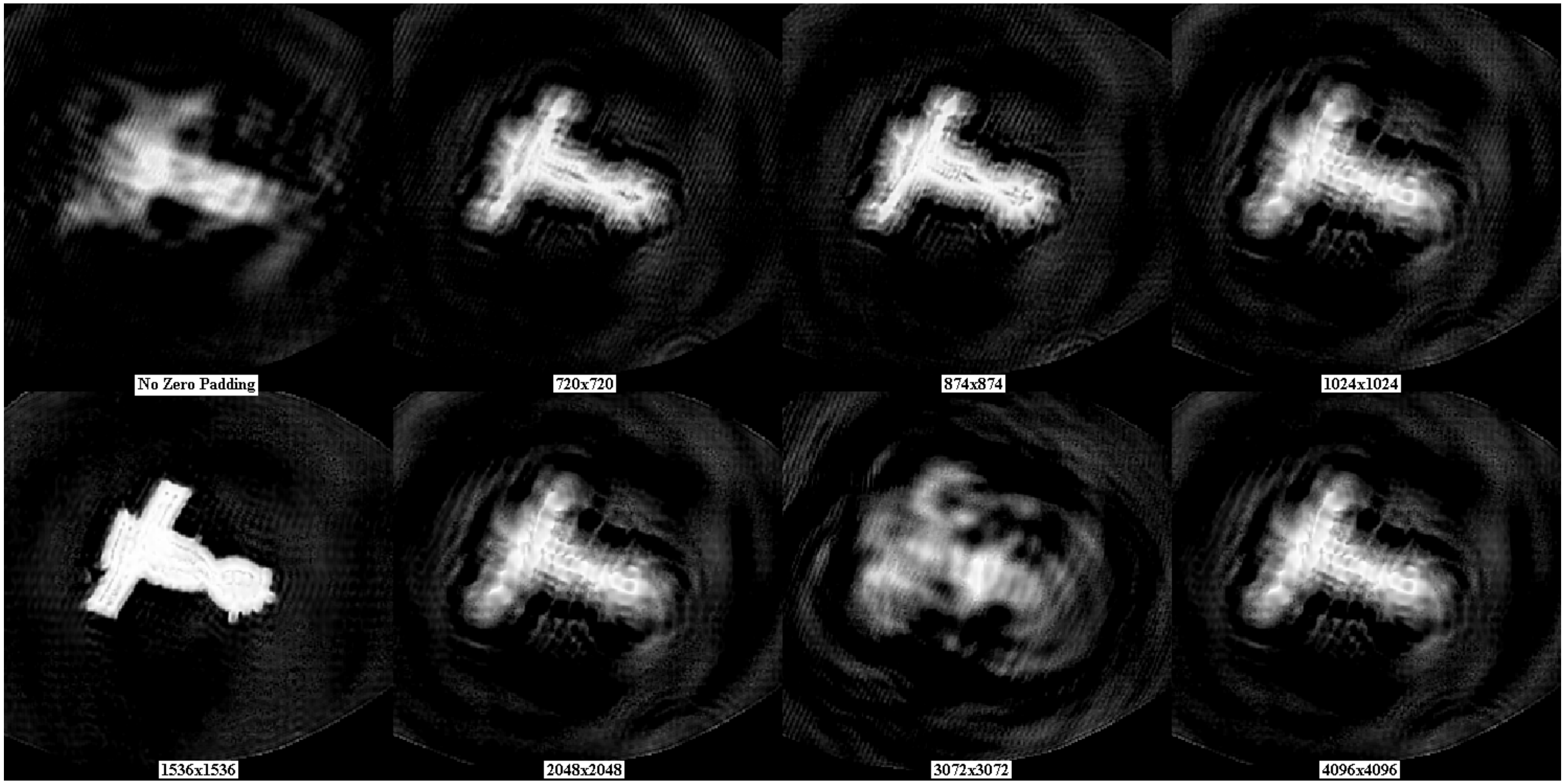

Figure 19: Silhouette reconstruction of the Soyuz spacecraft at 180.4 mm (0.5x GEO equivalent) using eight different amounts of zero padding, shown below each reconstruction.

Figure 20 shows the images captured at a distance of 358.2 mm (GEO altitude equivalent), used as inputs to the Matlab code whose silhouette reconstruction results with eight amounts of zero padding are shown in Figure 21 and Figure 22.

The silhouette reconstructions at this distance are clear at the zero padding amount of 720 x 720, with some of the larger instruments of the Soyuz spacecraft visible. Edges and corners of the GPS satellite and Soyuz spacecraft solar panels and main body are sharp. Inspecting the smallest resolvable feature on the bottom right of the Soyuz spacecraft, the resolution at this distance is estimated to be 36 microns (scaled 36 cm). Interestingly, the reconstruction clarity alternates between increase and decrease with increasing amounts of zero padding, although the 720 x 720 zero padding is the most clear.

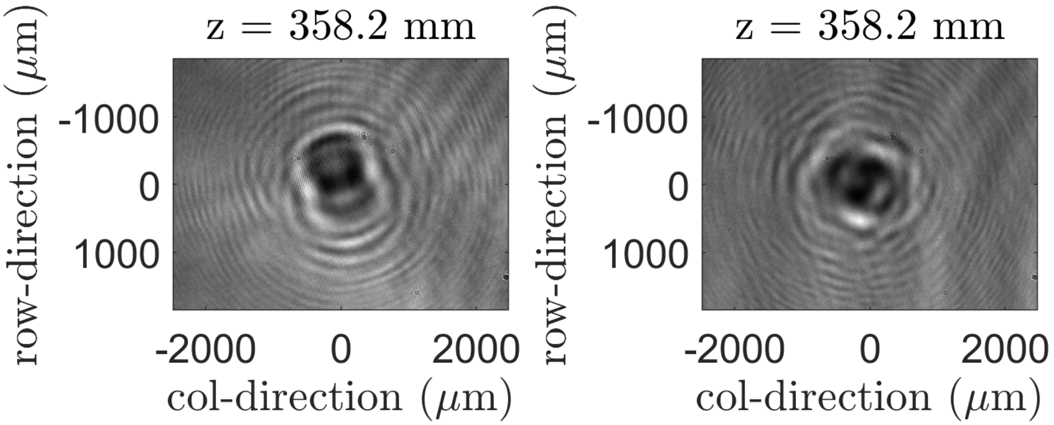

Figure 20: Laboratory data collected using the GPS (left) and Soyuz (right) targets at 358.2 mm (GEO altitude equivalent).

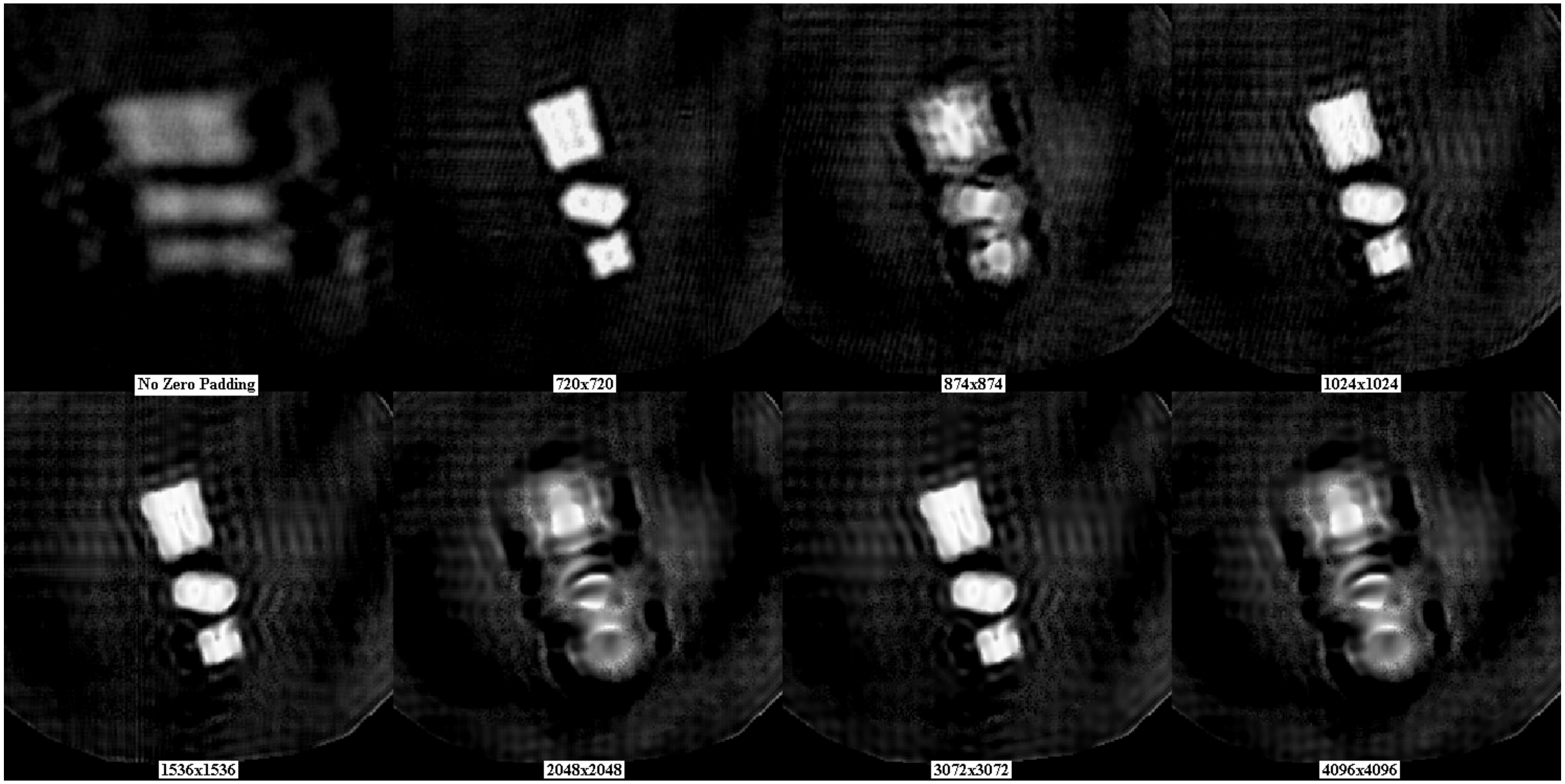

Figure 21: Silhouette reconstruction of the GPS satellite at 358.2 mm (GEO equivalent) using eight different amounts of zero padding, shown below each reconstruction.

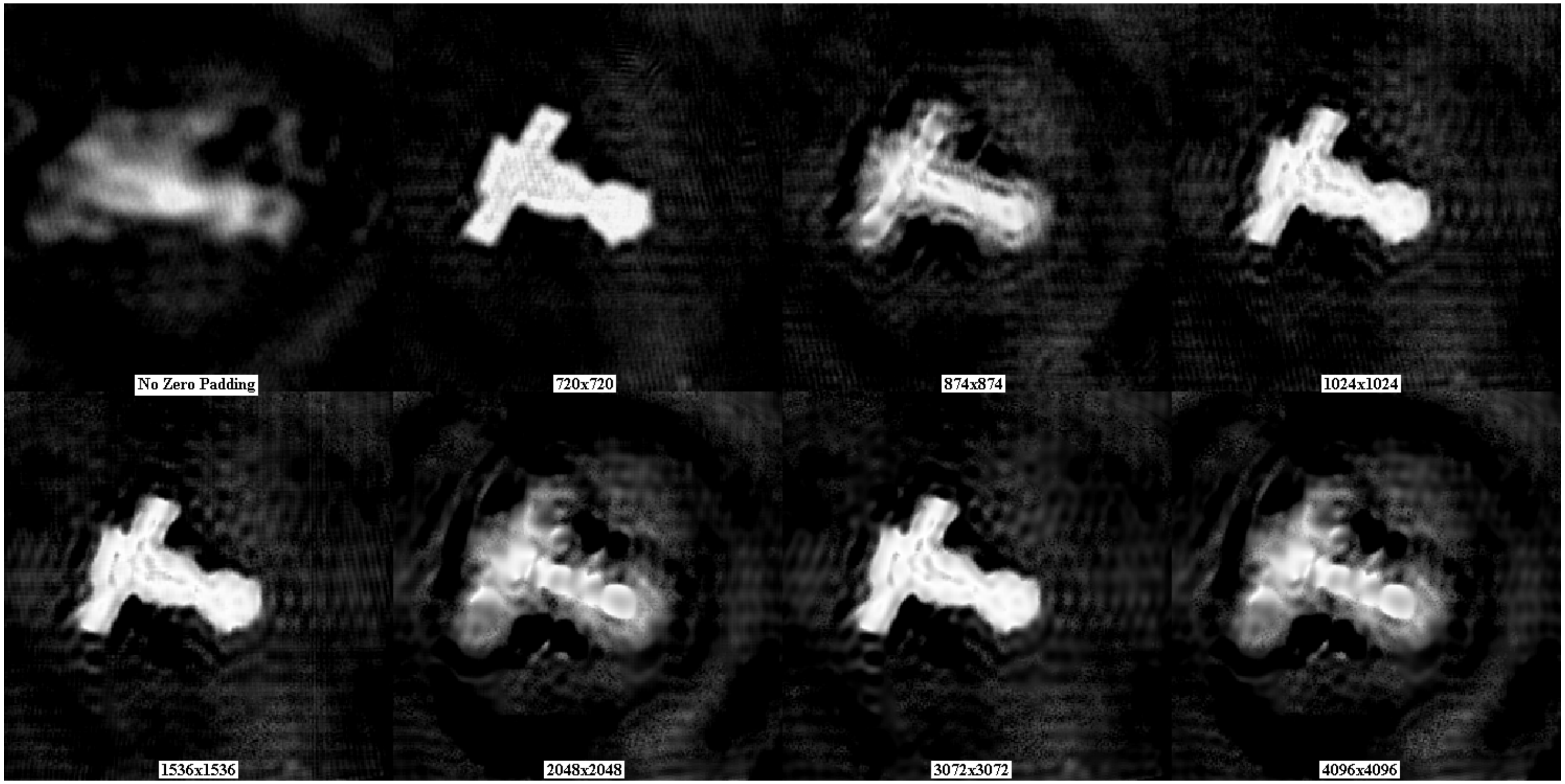

Figure 22: Silhouette reconstruction of the Soyuz spacecraft at 358.2 mm (GEO equivalent) using eight different amounts of zero padding, shown below each reconstruction.

Figure 23 shows the images captured at a distance of 536.0 mm (1.5x GEO altitude equivalent), used as inputs to the Matlab code whose silhouette reconstruction results with eight amounts of zero padding are shown in Figure 24 and Figure 25.

The silhouette reconstructions at this distance are most clear at the zero padding amount of 874 x 874, although only spacecraft main body and solar panels are resolvable. Main body and solar panel edges and corners are not sharp, but are not diffuse enough to prevent size estimation. Inspecting the gap between the back of Soyuz spacecraft and its solar panel, the resolution at this distance is estimated to be 91 microns (scaled 91 cm). As with the 358.2 mm reconstructions, the reconstruction clarity alternates between increase and decrease with increasing amounts of zero padding, although this ends at 2048 x 2048 instead of continuing through 4096 x 4096.

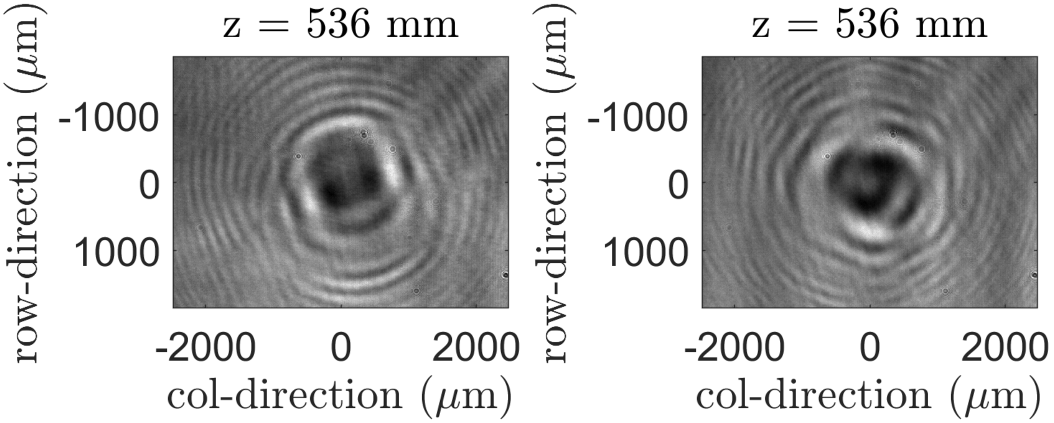

Figure 23: Laboratory data collected using the GPS (left) and Soyuz (right) targets at 536.0 mm (1.5x GEO altitude equivalent).

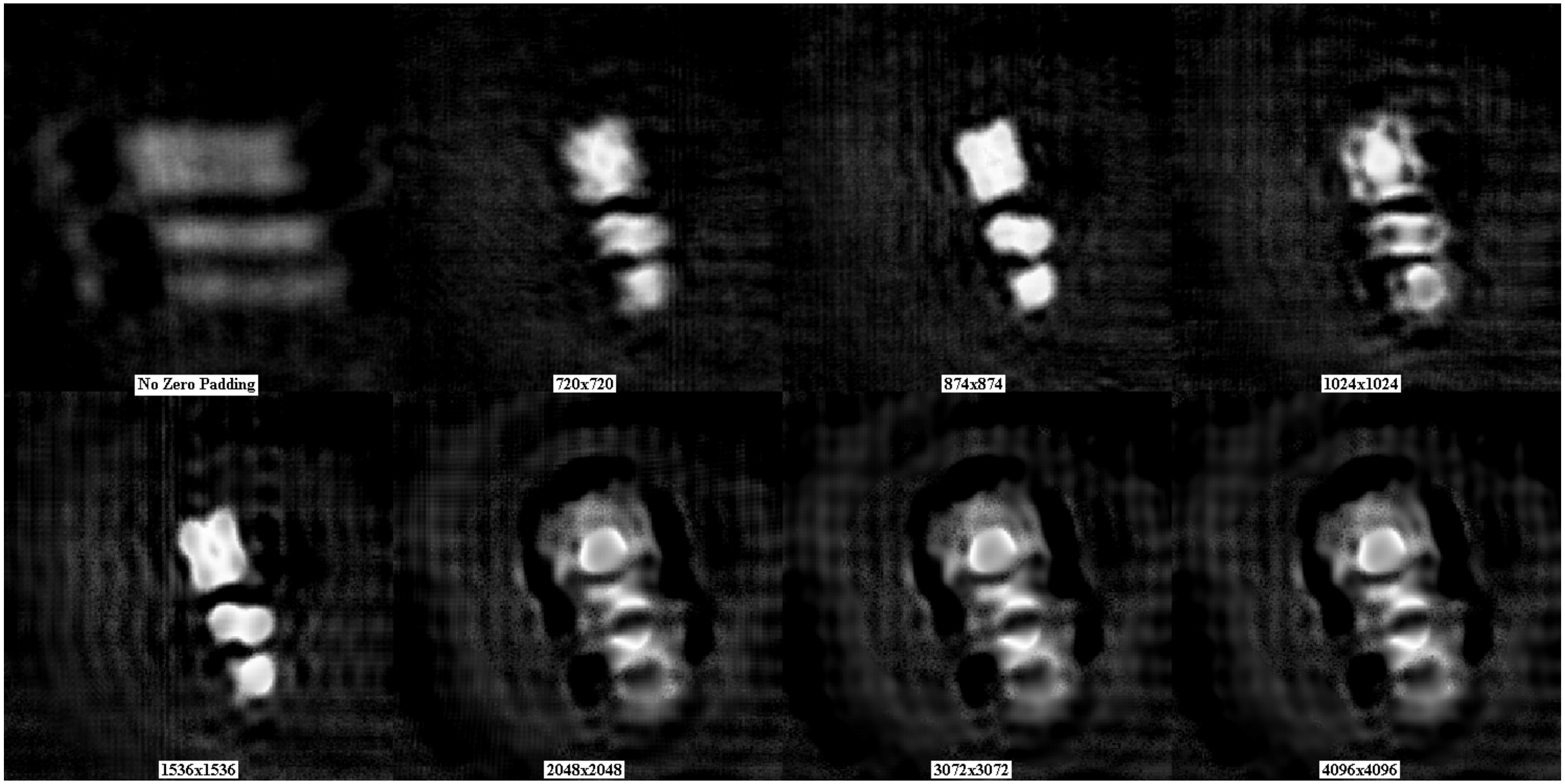

Figure 24: Silhouette reconstruction of the GPS satellite at 536.0 mm (1.5x GEO equivalent) using eight different amounts of zero padding, shown below each reconstruction.

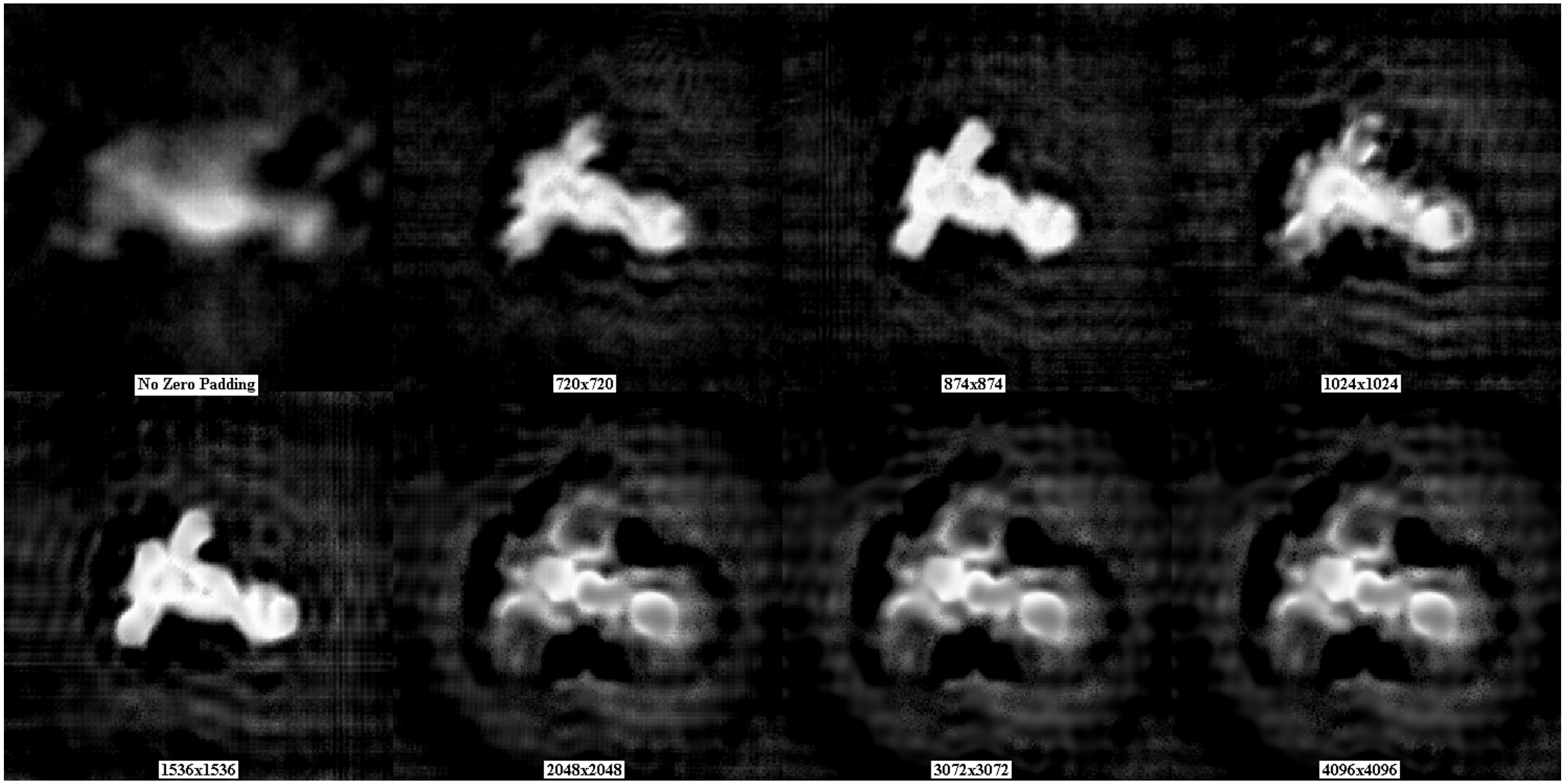

Figure 25: Silhouette reconstruction of the Soyuz spacecraft at 536.0 mm (1.5x GEO equivalent) using eight different amounts of zero padding, shown below each reconstruction.

Figure 26 shows the images captured at a distance of 713.8 mm (2.0x GEO altitude equivalent), used as inputs to the Matlab code whose silhouette reconstruction results with eight amounts of zero padding are shown in Figure 27 and Figure 28.

The silhouette reconstructions at this distance are most clear at the zero padding amount of 1536x1536, although only spacecraft main body and solar panels are barely resolvable. Main body and solar panel edges and corners are completely rounded, but are not diffuse enough to prevent size estimation. The Soyuz spacecraft appears somewhat warped near the ‘neck‘ between the two main body sections. Using the size of Soyuz solar panels, which are still resolvable, the resolution at this distance is estimated to be 154 µm (scaled 1.54 m). The reconstruction clarity increases with increasing amounts of zero padding until 1536 x 1536, then remains constant until an abrupt rapid decrease in clarity at 4096 x 4096.

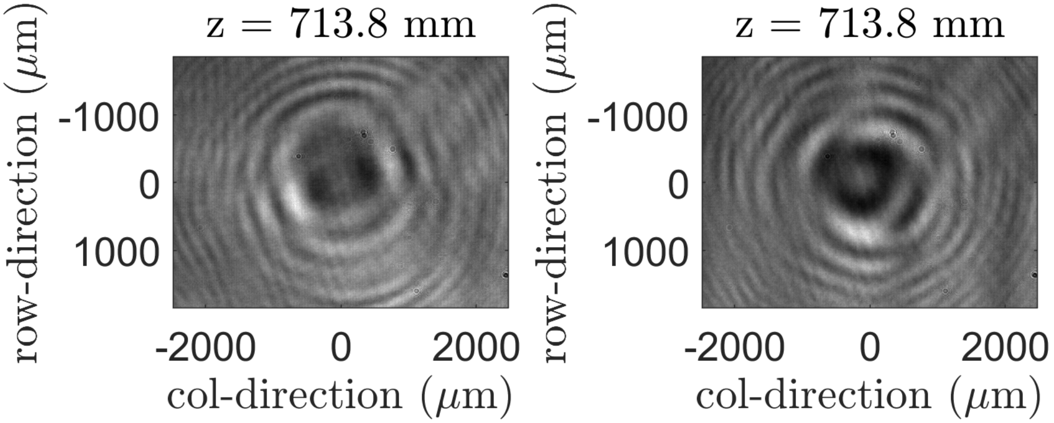

Figure 26: Laboratory data collected using the GPS (left) and Soyuz (right) targets at 713.8 mm (2.0x GEO altitude equivalent).

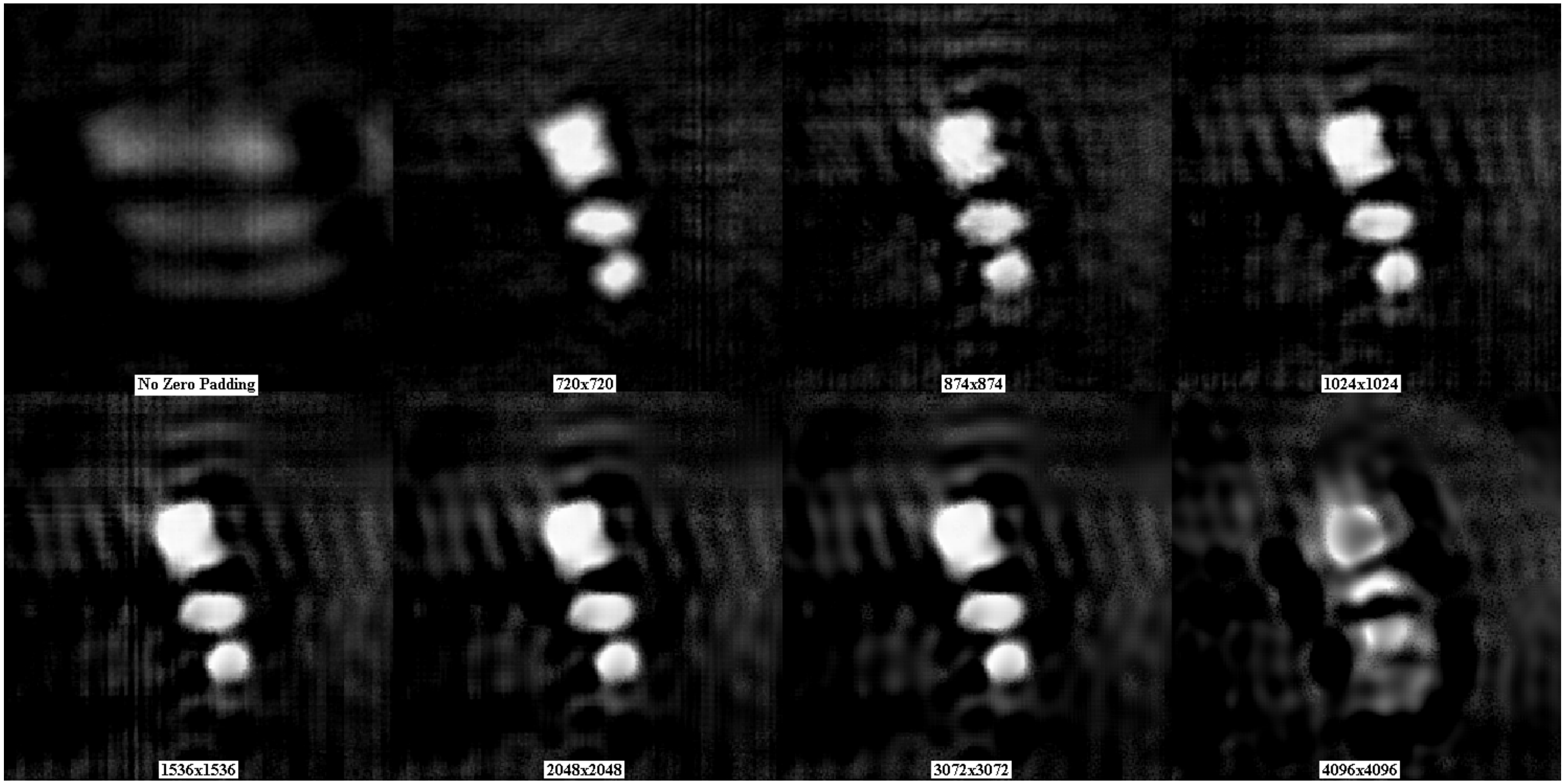

Figure 27: Silhouette reconstruction of the GPS satellite at 713.8 mm (2.0x GEO equivalent) using eight different amounts of zero padding, shown below each reconstruction.

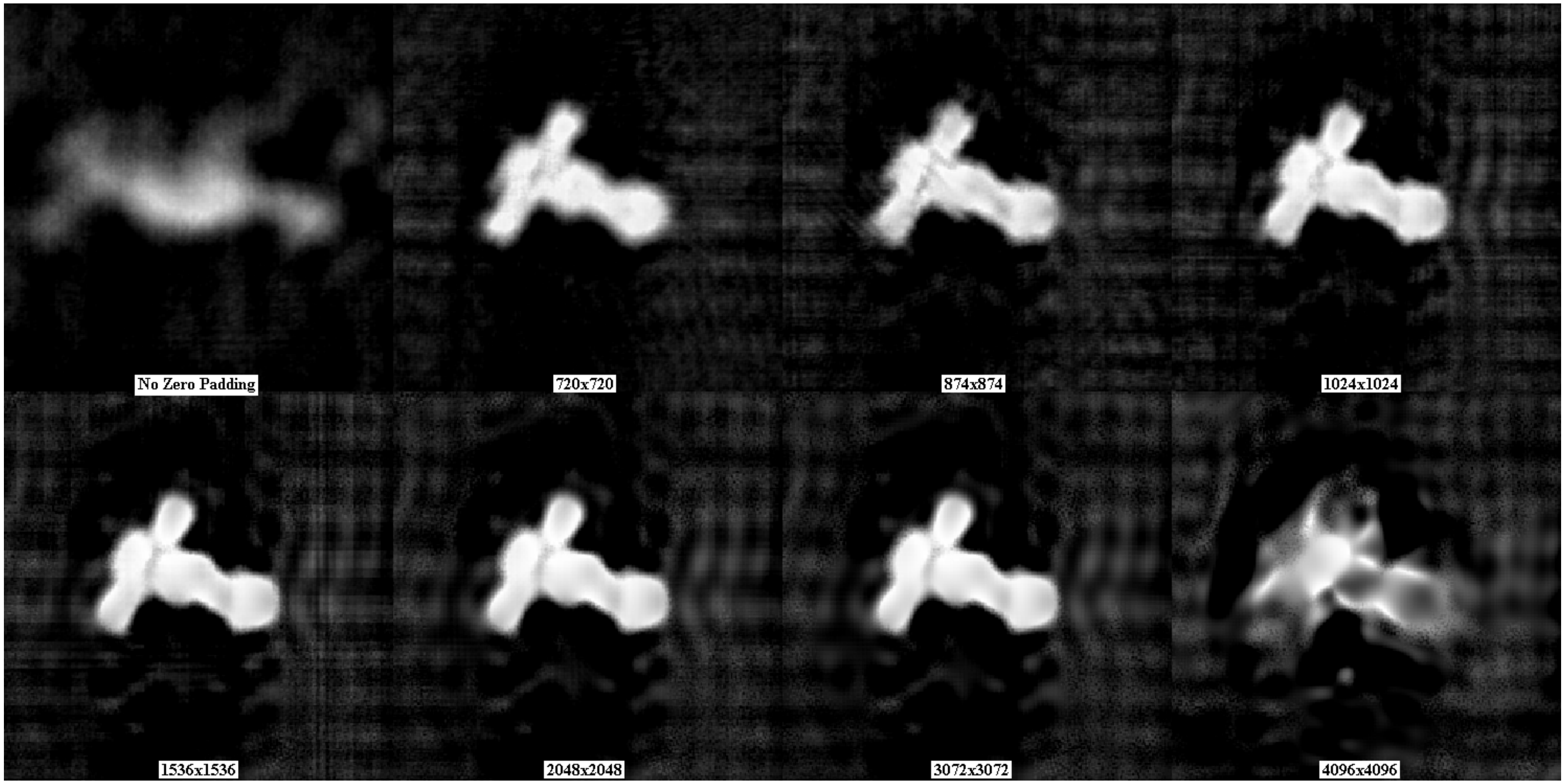

Figure 28: Silhouette reconstruction of the Soyuz spacecraft at 713.8 mm (2.0x GEO equivalent) using eight different amounts of zero padding, shown below each reconstruction.

4.2 Analysis

The resolution estimate, as well as the optimal amount of zero padding, at each distance are shown in Table 3.

The resolution, as expected, decreases with increased propagation distance, with the exception of the notable anomaly in the closest distance (53.4 mm), where the resulting reconstructions at 53.4 mm have a very noticeable spatial frequency distortion present at every amount of zero padding. This may be explained as resonance caused by interactions between the unwanted spatial frequency noise and the diffraction patterns. At the shortest measurement distance, the fringe separation distance in the spatial frequency noise is visible as roughly equal to the separation between the diffraction pattern fringes, giving weight to this possibility.

The resolution estimate at GEO is similar to the result in the 2020 Paxman experiment [3] at 36 cm compared to Paxman's 35 cm. A resolution of 36 cm is capable of providing very valuable information on the sate of spacecraft deployables, vehicle orientation, and the presence of small protruding instruments and antennas. While the resolution at twice GEO is approximately one and a half meters, this is still enough to provide valuable real world information, such as the size and deployment state of large solar arrays and the general form factor and orientation of a satellite of interest. However, at twice GEO the general form factor of the reconstructed silhouette becomes somewhat distorted in shape (other than through decreased resolution), most

Table 3: Resolution Estimates at Five Distances

Benchtop Distance (mm)	**Scaled Distance (km)**	**Optimal Zero Padding**	**Benchtop Resolution (μm)**	**Scaled Resolution (m)**
53.4	5340	1536 x 1536	154	1.54
180.4	18040 (0.5x GEO)	1536 x 1536	24	0.24
358.2	35820 (GEO)	720 x 720	36	0.36
536.0	53600 (1.5x GEO)	874 x 874	91	0.91
713.8	71380 (2.0x GEO)	1536 x 1536	154	1.54

notable at the ‘neck‘ between the two main body sections of the Soyuz spacecraft. When approaching future data collection, a question worth resolving is whether this is a result of a relatively limited view of the diffraction pattern, which grows far past the bounds of the photodetector array, as well as how much, if any, resolution increase that may give to each propagation distance. Since the Fresnel number of measurements at this distance and size of satellites is approximately 0.5, a strong possibility is that the limitations of the Fresnel approximation have been met. Modification of the silhouette reconstruction code to instead use the Fraunhofer approximation may give better results, and is a key factor of interest for future data collection at greater distances.

While the amount of zero padding needed for the best reconstruction is the same for three of the distances, a linear relationship is not seen between distance and required zero padding. Most interestingly, at 358.2 mm (GEO equivalent) in particular, is the cycling between increase and decrease in resolution as the amount of zero padding increases. The size of the array input to the Fourier transform functions is important, as zero padding past the data in the array results in interpolation in the frequency domain, and it is this interpolation that may be interacting with the diffraction to lead to these results. Additionally, the results without zero padding are in most cases completely unrecognizable, a result of the highly non-square aspect ratio of the input images, and the improved fast Fourier transform results from zero padding to a square array.

An inspection of the collected data reveals potential improvements through a change of laboratory equipment. Spatial frequency noise, noted above as a potential factor in optimal zero padding and the low resolution results of the closest measurement distance, is shown in every image of the target and flat field, a potential result of the HeNe laser source. This may be alleviated through use of an alternate broadband source, or collection of additional samples using the additional laser sources and stacking of the images before processing, an excellent starting point for future data collection and analysis. Visual artifacts, likely a result of pitting, dust, or other imperfections of the collimating lens or the camera's glass shield, are eliminated in part through pre-filtering, but are still valid targets for future data collection improvements.

V. Conclusions

The research conducted in this thesis analyzed resolution and distance limitations of a Synthetic Aperture Silhouette Imaging (SASI) system, which makes use of diffraction patterns cast to the ground by the occlusion of distant stars, for satellites at GEO and greater distances. A benchtop experiment was constructed to gather diffraction images which were scalable to up to twice GEO. Images were gathered using GPS satellite and Soyuz spacecraft targets and fed as input to a Matlab program which makes use of an iterative phase retrieval algorithm to reconstruct the original silhouettes. Images were processed using eight different amounts of zero padding, and the resulting reconstructions were analyzed to estimate resolution. Silhouettes at up to twice GEO scaled distance were successfully reconstructed, producing an estimated resolution of .36 meters at GEO and 1.54 meters at twice GEO. GEO results aligned with a previous 2020 experiment by Paxman [3] and all results demonstrated value in SASI data at GEO and beyond, reinforcing the potential for a fielded SASI system to fill a current gap in imaging capabilities for Space Domain Awareness.

5.1 Future Work

Numerous improvements to the benchtop experiment, through both data collection and processing, additional factors required for complete analysis of a fielded SASI system, and next steps towards SASI data gathering are all targets for future work.

The benchtop experiment could be targeted for improvements to eliminate unwanted artifacts and noise. Use of a more precise collimating lens could reduce diffraction artifacts at the imaging plane. A camera with a larger photodetector array, which could capture a wider diffraction pattern, may improve reconstruction results, particularly beyond GEO. Investigation of the relationship between extent of captured diffraction and resolution should be investigated, and may include a deeper analysis into the effect/requirement of zero padding or other pre-processing improvements such as further noise filtering.

Data collection using the additional laser sources, or a new broadband source, could also be used to examine the effect of spectral binning on resolution results. A broadband source in particular could eliminate the spatial noise seen in collected images and result in improved reconstruction results.

Another question to be answered is the relationship between array size, spacing, and telescope specs and the results from a silhouette reconstruction. A new benchtop experiment to model an array with variable spacing could be constructed, or data from the current setup pre-processed to simulate the results.

Importantly, the other major hurdles, namely the problem of alignment between equipment on the ground, satellite, and occluded stars, and the number of occultation opportunities available, must be explored to prove viability of a fielded system. Analysis of real-world viable ground sites plus an extensive charting of occultation opportunities using high fidelity star catalogues for satellites in various orbits is one avenue of approach, and inclusion of detector array size in the trade space and/or use of a mobile fielded system are additional variables to consider.

Finally, a large step in proving the use of SASI would be a field experiment to gather real satellite occlusion data. Prediction of easier (lower orbit) or larger (International Space Station) targets and an attempt at alignment is a potential starting point, and required alignment precision can be mitigated through use of a larger North-South array of telescopes.

Appendix A. Additional Laboratory Data

Figure 29 through Figure 32 contains the full collected laboratory data set, including dark frame and flat field images, removed from the main document due to limited use in the analysis.

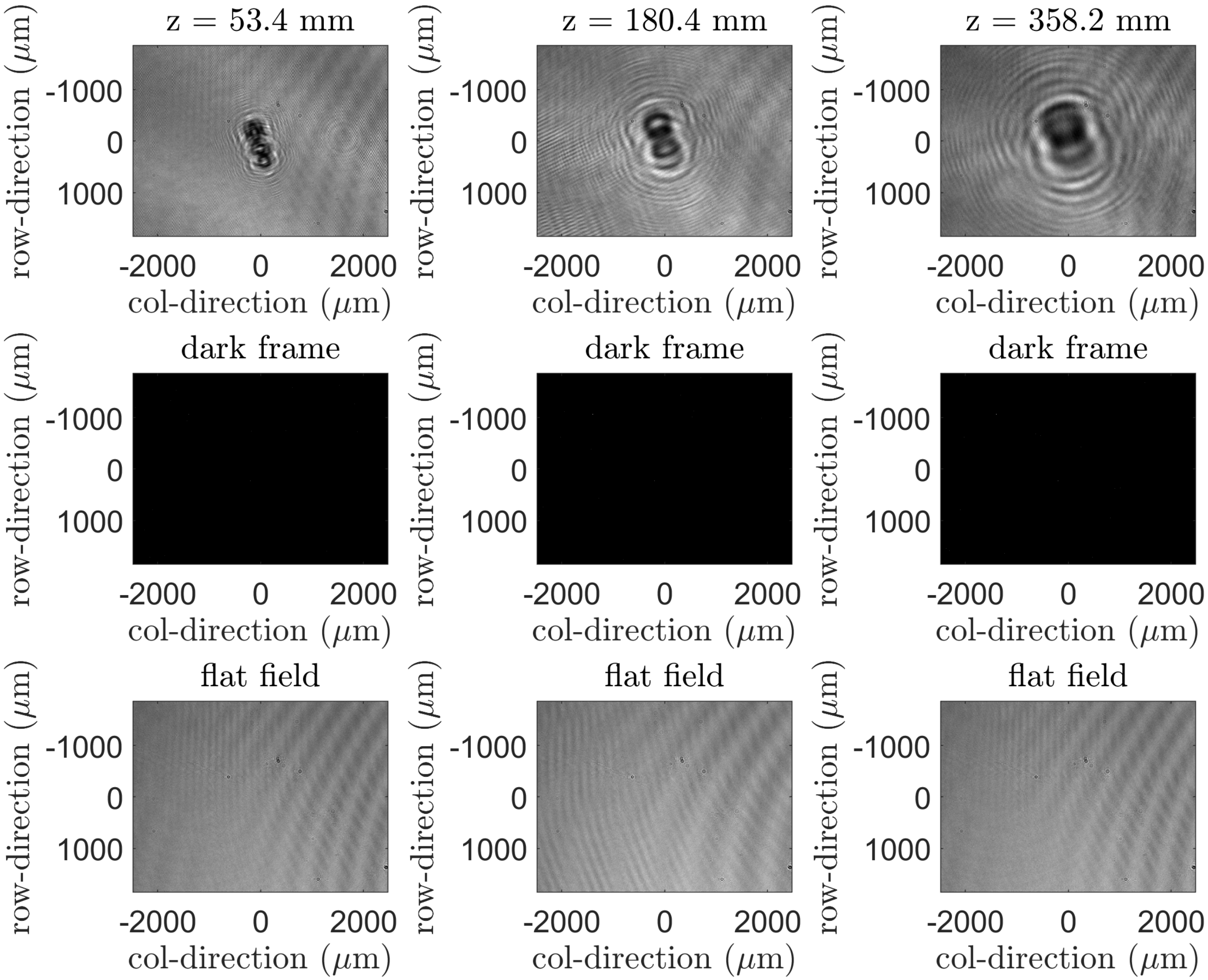

Figure 29: Laboratory data collected using the GPS target at (left to right) 53.4 mm (5340 km altitude equivalent), 180.4 mm (0.5x GEO equivalent), and 358.2 mm (GEO equivalent).

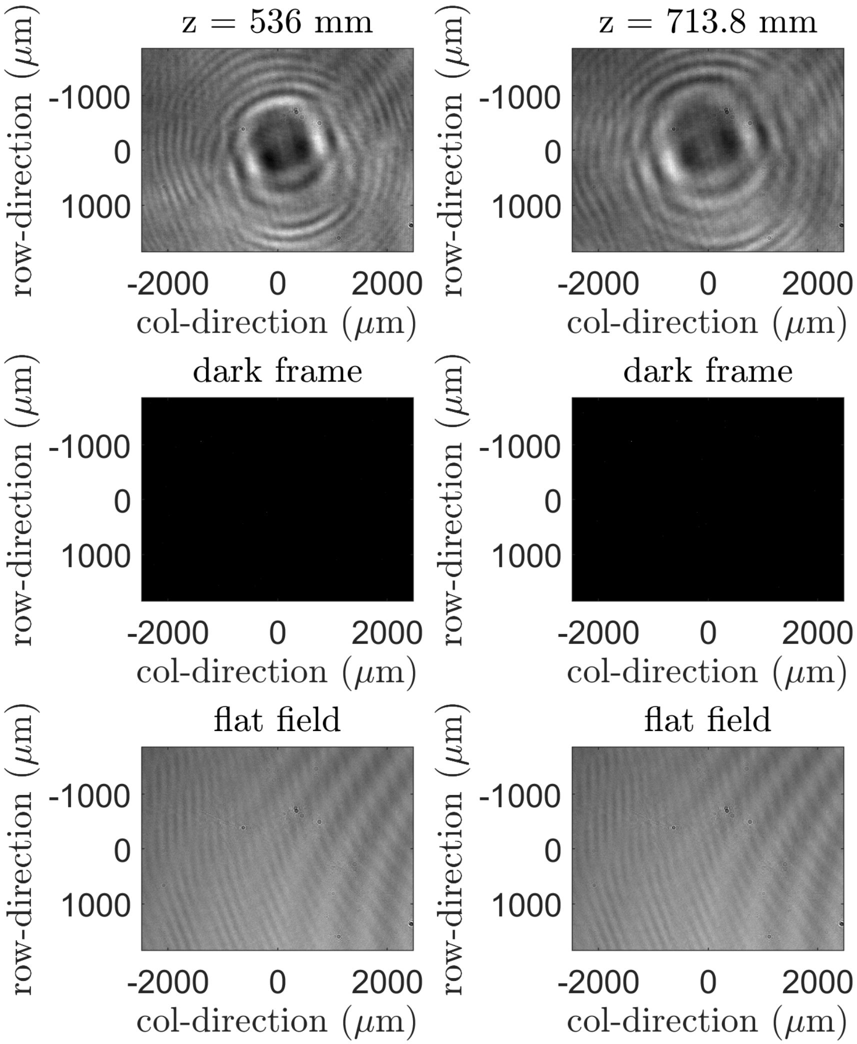

Figure 30: Laboratory data collected using the GPS target at (left) 536.0 mm (1.5x GEO equivalent), and (right) 713.8 mm (2.0x GEO equivalent).

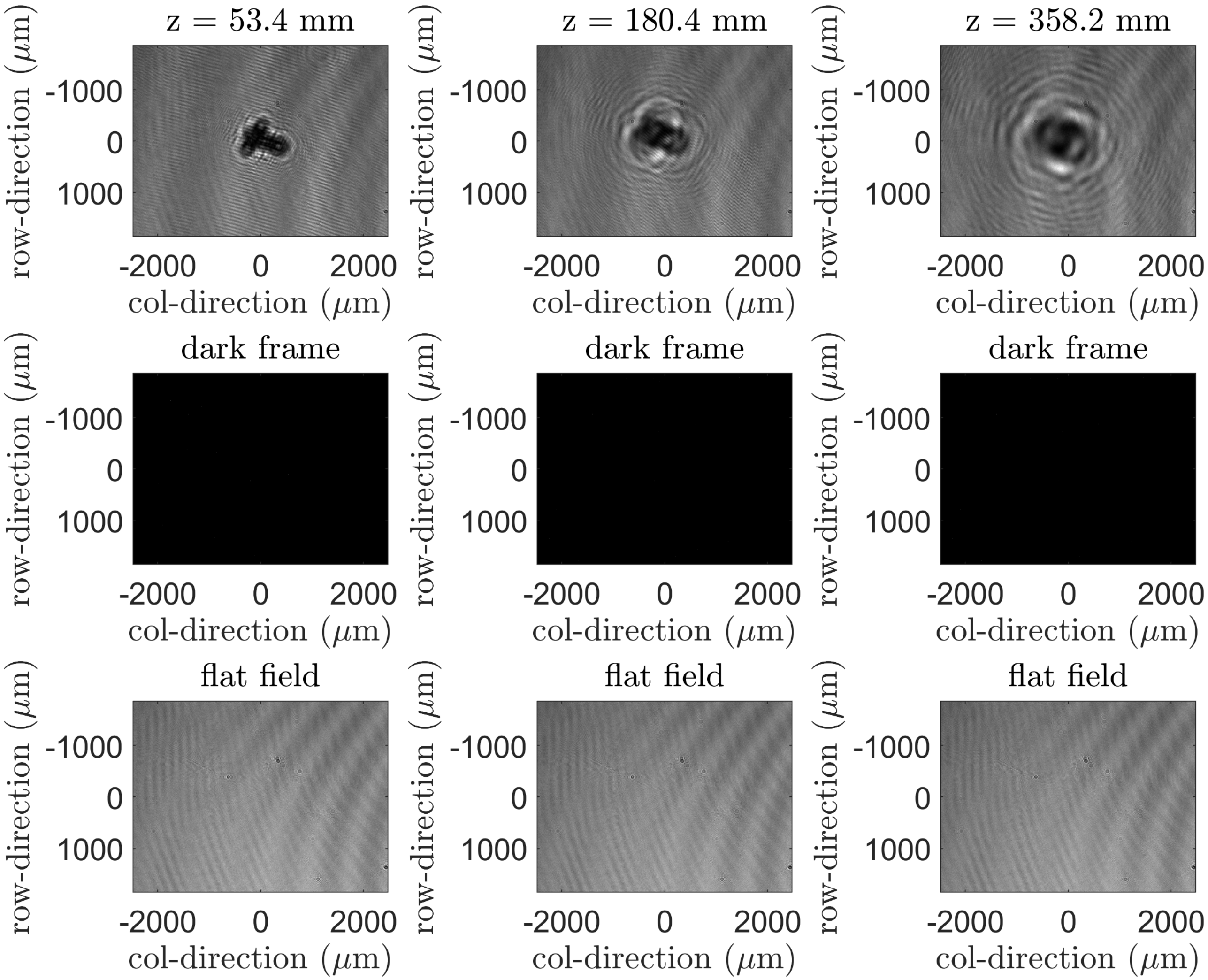

Figure 31: Laboratory data collected using the Soyuz target at (left to right) 53.4 mm (5340 km altitude equivalent), 180.4 mm (0.5x GEO equivalent), and 358.2 mm (GEO equivalent).

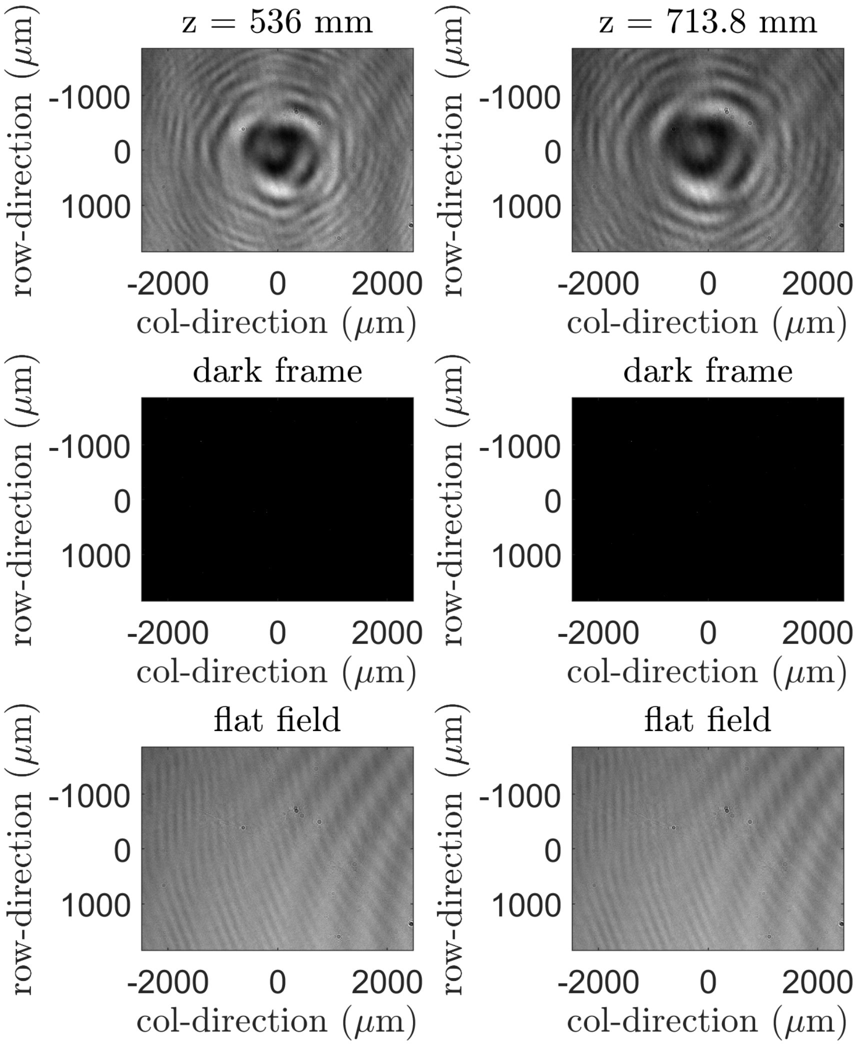

Figure 32: Laboratory data collected using the Soyuz target at (left) 536.0 mm (1.5x GEO equivalent), and (right) 713.8 mm (2.0x GEO equivalent).

Bibliography

1. R. H. Burns, J. J. Gamiz, V.and Dolne, J. Lambert, and S. Long. Shadow imaging of geo satellites. *Proceedings of the Society of Photo-Optical Instrumentation Engineers*, 5896, 2005.

2. R. G. Paxman. Synthetic-aperture silhouette imaging. *Proceedings of the Advanced Maui Optical and Space Surveillance Technologies Conference*, 2016.

3. R. G. Paxman, K. W. Gleichman, A. S. Iacchetta, and B. M. Jost. Synthetic-aperture silhouette imaging (sasi) laboratory demonstration. *Proceedings of the Imaging and Applied Optics Congress*, 2020.

4. J. Luu, L. Jiang, and B. Willard. Shadow imaging efforts at mit lincoln laboratory. *Proceedings of the Advanced Maui Optical and Space Surveillance Technologies Conference*, 2008.

5. Joseph W Goodman. *Introduction to Fourier optics*. New York: McGraw-Hill, 1996.

6. D. M. Douglas, B. R. Hunt, and D. G. Sheppard. Shadow imaging of geosynchronous satellites: Simulation, image reconstruction, and shadow prediction. *Proceedings of the Society of Photo-Optical Instrumentation Engineers*, 9982, 2016.

7. D. M. Douglas, B. R. Hunt, D. G. Sheppard, and A. Todoki. Recent developments in shadow imaging prediction. *Proceedings of the Advanced Maui Optical and Space Surveillance Technologies Conference*, 2017.

8. D. M. Douglas, B. R. Hunt, and D. G. Sheppard. Recent developments in shadow imaging prediction. *Proceedings of the Advanced Maui Optical and Space Surveillance Technologies Conference*, 2018.
9. Richard G. Paxman, David A. Carrara, Paul D. Walker, and Nicolas Davidenko. Silhouette estimation. *J. Opt. Soc. Am. A*, 31(7):1636–1644, Jul 2014.
10. Patrick J. McNicholl and Peter N. Crabtree. Statistical bounds and maximum likelihood performance for shot noise limited knife-edge modeled stellar occultation. In Jean J. Dolne, Thomas J. Karr, and Victor L. Gamiz, editors, *Unconventional Imaging and Wavefront Sensing 2014*, volume 9227, pages 41 – 54. International Society for Optics and Photonics, SPIE, 2014.
11. Dennis M. Douglas, Bobby R. Hunt, and David G. Sheppard. Resolution limits for shadow imaging of geosynchronous satellites: analytic and simulated approaches. In Jean J. Dolne and Rick P. Millane, editors, *Unconventional and Indirect Imaging, Image Reconstruction, and Wavefront Sensing 2017*, volume 10410, pages 173 – 183. International Society for Optics and Photonics, SPIE, 2017.
12. Marc W. Buie, Simon B. Porter, Peter Tamblyn, Dirk Terrell, Alex Harrison Parker, David Baratoux, Maram Kaire, Rodrigo Leiva, Anne J. Verbiscer, Amanda M. Zangari, François Colas, Baïdy Demba Diop, Joseph I. Samaniego, Lawrence H. Wasserman, Susan D. Benecchi, Amir Caspi, Stephen Gwyn, J.J. Kavelaars, Adriana C. Ocampo Uría, Jorge Rabassa, M. F. Skrutskie, Alejandro Soto, Paolo Tanga, Eliot F. Young, S. Alan Stern, Bridget C. Andersen, Mauricio E. Arango Pérez, Anicia Arredondo, Rodolfo Alfredo Artola, Abdoulaye Bâ, Romuald Ballet, Ted Blank, Cheikh Tidiane Bop, Amanda S. Bosh, Matías Aarón Camino López, Christian M. Carter, J. H. Castro-Chacón, Alfonso Caycedo Desprez, Nicolás Caycedo Guerra, Steven J. Conard, Jean-Luc

Dauvergne, Bryan Dean, Michelle Dean, Josselin Desmars, Abdou Lahat Dieng, Mame Diarra Bousso Dieng, Omar Diouf, Gualbert Séraphin Dorego, David W. Dunham, Joan Dunham, Hugo A. Durantini Luca, Patrick Edwards, Nicolas Erasmus, Gayane Faye, Mactar Faye, Lucas Ezequiel Ferrario, Chelsea L. Ferrell, Tiffany J. Finley, Wesley C. Fraser, Alison J. Friedli, Julián Galvez Serna, Esteban A. Garcia-Migani, Anja Genade, Kai Getrost, Ricardo A. Gil-Hutton, German N. Gimeno, Eli Joseph Golub, Giovanni Francisco González Murillo, Michael D. Grusin, Sebastian Gurovich, William H. Hanna, Santiago M. Henn, P. C. Hinton, Paul J. Hughes, John David Josephs Jr, Raul Joya, Joshua A. Kammer, Brian A. Keeney, John M. Keller, Emily A. Kramer, Stephen E. Levine, Carey M. Lisse, Amy J. Lovell, Jason A. Mackie, Stanislav Makarchuk, Luis E. Manzano, Salma Sylla Mbaye, Modou Mbaye, Raul Roberto Melia, Freddy Moreno, Sean K. Moss, Diene Ndaiye, Mapathe Ndiaye, Matthew J. Nelson, Catherine B. Olkin, Aart M. Olsen, Victor Jonathan Ospina Moreno, Jay M. Pasachoff, Mariana Belen Pereyra, Michael J. Person, Giovanni Pinzón, Eduardo Alejandro Pulver, Edwin A. Quintero, Jeffrey R. Regester, Aaron Caleb Resnick, Mauricio Reyes-Ruiz, Alex D. Rolfsmeier, Trina R. Ruhland, Julien Salmon, Pablo Santos-Sanz, Marcos Ariel Santucho, Diana Karina Sepúlveda Niño, Amanda A. Sickafoose, José S. Silva, Kelsi N. Singer, Joy N. Skipper, Stephen M. Slivan, Rose J. C. Smith, Julio C. Spagnotto, Andrew W. Stephens, Samuel D. Strabala, Francisco J. Tamayo, Henry B. Throop, Andrés David Torres Cañas, Labaly Toure, Alassane Traore, Constantine C. C. Tsang, Jake D. Turner, Santiago Vanegas, Roger Venable, John C. Wilson, Carlos A. Zuluaga, and Jorge I. Zuluaga. Size and shape constraints of (486958) arrokoth from stellar occultations. *The Astronomical Journal*, 159(4):130, 2020.

13. F. Braga-Ribas, B. Sicardy, J. L. Ortiz, C. Snodgrass, F. Roques, R. Vieira-

Martins, J. I. B. Camargo, M. Assafin, R. Duffard, E. Jehin, J. Pollock, R. Leiva, M. Emilio, D. I. Machado, C. Colazo, E. Lellouch, J. Skottfelt, M. Gillon, N. Ligier, L. Maquet, G. Benedetti-Rossi, A. Ramos Gomes Jr, P. Kervella, H. Monteiro, R. Sfair, M. El Moutamid, G. Tancredi, J. Spagnotto, A. Maury, N. Morales, R. Gil-Hutton, S. Roland, A. Ceretta, S. h. Gu, X. b. Wang, K. Harpsøe, M. Rabus, J. Manfroid, C. Opitom, L. Vanzi, L. Mehret, L. Lorenzini, E. M. Schneiter, R. Melia, J. Lecacheux, F. Colas, F. Vachier, T. Widemann, L. Almenares, R. G. Sandness, F. Char, V. Perez, P. Lemos, N. Martinez, U. G. Jørgensen, M. Dominik, F. Roig, D. E. Reichart, A. P. LaCluyze, J. B. Haislip, K. M. Ivarsen, J. P. Moore, N. R. Frank, and D. G. Lambas. A ring system detected around the centaur (10199) chariklo. *Nature*, 508(7494):72–75, 2014.

14. Edmund Optics. Understanding spatial filters, 2022. Last accessed 09 February 2022.

REPORT DOCUMENTATION PAGE

Form Approved
OMB No. 0704–0188

1. REPORT DATE *(DD–MM–YYYY)* 07–03–2022	**2. REPORT TYPE** Master's Thesis	**3. DATES COVERED** *(From — To)* Sept 2020 — Mar 2022

4. TITLE AND SUBTITLE

Synthetic Aperture Silhouette Imaging
for Space Domain Awareness

5a. CONTRACT NUMBER

5b. GRANT NUMBER

5c. PROGRAM ELEMENT NUMBER

6. AUTHOR(S)

Tuck, Lester, L. IV, Capt, USAF

5d. PROJECT NUMBER

5e. TASK NUMBER

5f. WORK UNIT NUMBER

7. PERFORMING ORGANIZATION NAME(S) AND ADDRESS(ES)

Air Force Institute of Technology
Graduate School of Engineering and Management (AFIT/EN)
2950 Hobson Way
WPAFB OH 45433-7765

8. PERFORMING ORGANIZATION REPORT NUMBER

AFIT-ENY-MS-22-M-314

9. SPONSORING / MONITORING AGENCY NAME(S) AND ADDRESS(ES)

10. SPONSOR/MONITOR'S ACRONYM(S)

11. SPONSOR/MONITOR'S REPORT NUMBER(S)

12. DISTRIBUTION / AVAILABILITY STATEMENT

DISTRIBUTION STATEMENT A:
APPROVED FOR PUBLIC RELEASE; DISTRIBUTION UNLIMITED.

13. SUPPLEMENTARY NOTES

14. ABSTRACT

A gap exists in imaging capabilities necessary for Space Domain Awareness, at Geostationary Equatorial Orbit (GEO) distances and beyond. Synthetic Aperture Silhouette Imaging (SASI), which resolves a space object's silhouette with measurements of the diffraction pattern cast by the object's occultation of a distant star, provides a new method that may be used to characterize these satellites. This research analyzes the reconstruction of satellite silhouettes using data from a scaled benchtop experiment to evaluate the distance and resolution limitations of SASI at distances equal to and beyond GEO. Diffraction patterns of two satellite silhouette targets are captured at various scaled distances and fed to Matlab code which utilizes an iterative phase retrieval algorithm to estimate the original silhouettes. Resolutions of 36 centimeters at GEO altitude and 1.54 meters at twice GEO altitude were obtained, and identified measurement improvements show potential for even greater resolution. These results demonstrate the value of SASI as a tool which can provide valuable information of a satellite of interest and fill in the SDA imaging capability gap.

15. SUBJECT TERMS

diffraction, fresnel diffraction, geostationary equatorial orbit (GEO), occultation, satellites, synthetic aperture silhouette imaging (SASI), space domain awareness (SDA)

16. SECURITY CLASSIFICATION OF:			**17. LIMITATION OF ABSTRACT**	**18. NUMBER OF PAGES**	**19a. NAME OF RESPONSIBLE PERSON**
a. REPORT	**b. ABSTRACT**	**c. THIS PAGE**			Dr. Andrew S. Keys, AFIT/ENY
U	U	U	UU	64	**19b. TELEPHONE NUMBER** *(include area code)* (937) 255-3636 x4747; Andrew.Keys@afit.edu

Standard Form 298 (Rev. 8–98)
Prescribed by ANSI Std. Z39.18